Chapter 1

Introduction

The interactions between material and surrounding environment are of highly interest in both fundamental science and technology. One of the most illustrating cases is liquid crystal thin films. Liquid crystals, which possess both the properties of solid and the flow properties of liquid, form a complex thin film system. The molecular arrangements in various phases of liquid crystals make the interactions between liquid crystal-polymer molecules, liquid crystal-liquid crystal, and liquid crystal-external applied field complicated and difficult to describe clearly. Furthermore, the interactions between liquid crystals and external fields, such as electric field, magnetic field and light field, are essential to many practical applications. The most well-known application that deeply influence daily life are the liquid crystal displays (LCDs), which are based on the electro-optic properties of liquid crystals.

In electro-optic applications, the LC molecules are driven by an applied external field and reorient by the switching field. As a result, the induced variation of the optical anisotropy modulates the polarization states of the incident light. This electro-optic effect essentially reflects the averaged behaviors of all liquid crystal molecules. However, the different molecular fragments may play various roles in the reorientation process. Therefore, further understanding about how the inter-molecular and intra-molecular motions influence the macroscopic electro-optical switching dynamics is highly required. However, the investigation of molecular conformations and arrangements in equilibrium and during molecular transient motion is still a difficult task in liquid crystal science. In this thesis, we study the field-induced reorientation dynamics of liquid crystal thin films,

including a nematic liquid crystal twisted pi-cell and surface stabilized ferroelectric liquid crystals, with submolecular specificity.

From the view point of realistic application, the fast electro-optic response of LCDs is a basic requirement for video-rate applications. The issue of fast response may be solved by new device structures, or developing novel liquid crystal materials. Base on the consideration of the display fabrication processes, a slight modification on an existing device structure, which can benefit the response speeds greatly, is attractive due to its low cost. In this regard, the nematic twisted pi-cell[1] represents such a successful approach. By introducing a twisted structure to the conventional pi-cell, the response time is significantly reduced from more than 10 ms to about 2 ms, which is unachievable by other geometries of nematic LCD.

Although the response time of a twisted pi-cell can be push to milliseconds scale, it almost reaches the limit of nematic LC. Ferroelectric smectic C* liquid crystals are one of the most promising liquid crystal materials with a notable response time of microseconds. Ferroelectricity in liquid crystals was first discovered by Robert B. Mayer and co-workers in 1975,[2] while the invention of surface stabilized ferroelectric liquid crystal (SSFLC) devices[3] by N. A. Clark and S. T. Lagerwall initiated the wide application of FLC. The advantages of SSFLC, such as fast response, bistability and optical memory,[4] brighten the prospects of next-generation FLC displays, and therefore open a rather rich research field.

The vibrational spectroscopy is employed to investigate the field-induced molecular reorientation dynamics of a nematic twisted pi-cell and SSFLC, owing to the high sensitivity in reflecting the bonding and arrangement of molecular segments. In this study, we applied the infrared absorption and Raman scattering techniques to investigate the LC thin films. The IR and Raman spectra can provide valuable information about the conformation and orientational motions of individual segments of LC molecules, in which the molecular fragments can be identified owing to the 'fingerprinting' capability of IR and Raman spectroscopy.

Since the transient behavior of a LC molecular system during a dynamic switching process is most interested in this study, a time-resolved scheme with a

microsecond time resolution was developed with vibrational spectroscopies. Over past years, many different approaches have been proposed to perform the time-resolved spectroscopic measurements. Asynchronous time-resolved spectroscopy[5] is employed to study a nematic twisted pi-cell and an SSFLC. However, as the time-resolved scheme is combined with a polarization dependent measurement, the data acquisition is very time consuming. To improve the data-taking efficiency of time-resolved IR spectroscopy, we constructed a multichannel time-resolved asynchronous FTIR.[6] We applied the multichannel time-resolved system to study the field-induced reorientation dynamics of a neat FLC material and an FLC mixture.

Two dimensional (2D) correlation spectroscopy is a technique where the spectral intensity is plotted as a function of two independent spectral variables.[7] By spreading peaks along the second spectral dimension, one can gain advantage to sort out complex or overlapped spectral features that normally cannot be detected via the conventional spectroscopy. Owing to the enhancement of spectral resolution and sensitivity of perturbation-induced spectral variation, the 2D correlation analysis is introduced into the IR spectroscopic studies of the SSFLCs. The intramolecular correlated motions in a dc field and during a field-induced reorientation process thus can be studied in detail.

This thesis is organized as follows: Chapter 2 describes basic properties of LC materials and the structures of nematic twisted pi-cell and SSFLC.[8] The vibrational spectroscopies used in this thesis including IR spectrum and Raman Spectrum and asynchronous time-resolved scheme are introduced in Chapter 3.[9] The constructed multichannel time-resolving system and the principles of 2D correlation spectroscopy are also depicted. Chapter 4 and 5 present the time-resolved vibrational spectroscopy of the molecular reorientation dynamics in a twist pi-cell and an SSFLC mixture. In Chapter 6, the simulations of the 2D correlation spectroscopy are introduced and are employed to study the phase transition-induced and field-induced molecular reorientations of a neat FLC material. Chapter 7 presents the interpretations of the 2D IR spectroscopy of an

electro-optical switching SSFLC mixture. Finally a conclusion and future prospects are drawn.

Chapter 2

Pi Cell and Surface Stabilized

Ferroelectric Liquid Crystals

In this chapter, a brief description about the properties of liquid crystals is given. The first three sections depict the structures and properties of the nematic liquid crystal twisted pi-cell and surface stabilized ferroelectric liquid crystals. The importance of the study of the field-induced reorientation on a submolecular scale is elucidated in the last section.

2.1 Liquid Crystals

Liquid crystals (LC) are anisotropic fluids, with thermodynamically stable phases between the isotropic liquids and the crystalline solids. The liquid crystal phases can be further divided into several various subphases, depending on the order of the molecular system. There are two main liquid crystal phases: the *nematic* phase which exhibits orientational order and no positional order, and the *smectic* phase which exhibits both orientational and partial positional order.[10-12]

2.1.1 Liquid Crystal Phases

Liquid crystalline phases can be formed by many different types of molecules which differ widely in their structure. The typical LC molecular shapes are complicated, which can include the rod-like, discotic-like and the sanidic-like shapes. In this thesis, the rod-like shape molecules are of main interest. The orientation of a rod-like molecule can be described by introducing two local axes,

one parallel to the molecule known as *long axis*, and one perpendicular to it known as *short axis*. In general the molecules tend to align parallel to each other.

Nematic Phase

The nematic phase possesses an orientational order, but no positional order in a long range. In the nematic phase the molecular long axes are aligned, resulting in an averaged direction which is generally denoted with a unit vector n called *director* (see Fig. 2.1). The orientation of the director represents the direction of the optic axis of the molecular system. The nematic phase is optically uniaxial due to the fact that although the molecular long axis is somewhat oriented, but all the directions perpendicular to the director are equivalent.

On lowering the temperature of a nematic phase, additional orders such as positional order may appear. This can lead to a layered structure in the smectic phase and can be regarded as two dimensional liquids.
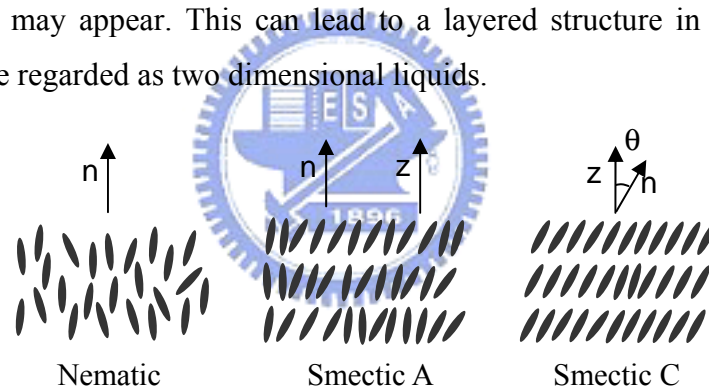
FIG. 2.1. Molecular arrangements in the nematic, SmA and SmC phases.

Smectic A Phase

In the smectic A phase (SmA), besides the orientational order, there exists a degree of positional order. The molecules are oriented more or less parallel to each other and their position is ordered in layers with the layer spacing approximately equal to the molecular length, forming the so-called *smectic layers* (see Fig. 2.1). The director n in the SmA phase is parallel to the *layer normal z* and determines the optic axis of the system. Inside the layers, molecules are movable and the molecular positions in adjacent layers are not correlated. Smectic layers are

flexible and can slide over each other. Uniformity of the layers can be easily distorted but the interlayer spacing tends to be preserved. The SmA phase, similar to the nematic phase, is optically uniaxial.

Smectic C Phase

The Smectic C phase (SmC) possesses both orientational and positional orders. The molecules in the SmC phase are also arranged in layers, but are not free to rotate along their long axes. The molecular long axes are tilted in a preferred direction with respect to the layer normal, in which the tilt directions of the molecules correlate in neighboring layers (see Fig. 2.1). The angle between the director *n* and the layer normal *z* defines the *tilt angle* of the material and is denoted as θ. The director is confined to a conical surface with the conic axis along the layer normal. The movement of the director is strictly limited to the orientations defined in space by the *smectic cone*. In principle, the SmC phase is optically biaxial, however, under specific circumstances it may form a uniaxial configuration.

In addition to the phases described above, there exists other LC phases. Various liquid crystals, especially mixtures, usually have more than one LC phase. Typically the phase sequence is a function of the temperature, say as following: (high temperature) isotropic phase I – N – SmA – SmC –Cr crystalline phase (low temperature). The order of the phases always follows the rule that more ordered phases occur at lower temperatures than less ordered phases.

2.1.2 Chirality in Liquid Crystals

A molecule becomes chiral if mirror symmetry elements are absent. The chiral molecule and its mirror image cannot be superimposed by any translations or rotations. Some molecules become chiral due to presence of a carbon atom, bonded to four distinct groups, serves as a *chiral center*. In liquid crystals chirality can be introduced in two ways. One is to introduce directly within the LC molecule by

incorporation of chiral centers, thus forming a single-component chiral material. Another way, more popular for applications, is to add a small amount of chiral dopant molecules into an achiral host phase, making the mixture exhibit induced chirality. The dopant used may have a liquid crystalline phase or not. Chiral phases are usually labeled by an asterisk "*" following the phase symbol.

Chiral Nematic Phase – N*

Doping chiral molecules into the achiral molecules in the nematic phase can form a so-called chiral nematic N* phase which possess twisted structure. Therefore the director in the N* phase, instead of being uniformly oriented, rotates in space about an axis perpendicular to *n* and forms a helical structure (*helix*) (see Fig. 2.2). The distance, in which the director makes a full 2π radians rotation along the helix axis, is called *helical pitch p*. Typically the pitch can vary from a few hundred nanometers (short pitch) to several micrometers (long pitch), which is mainly determined by the concentration of the dopant in the mixture. The chiral nematic twist can be either *right-* or *left-handed*, depending on the configuration of chiral elements within the molecule. Generally a positive pitch refers to a right-handed and a negative pitch to a left-handed helical superstructure.
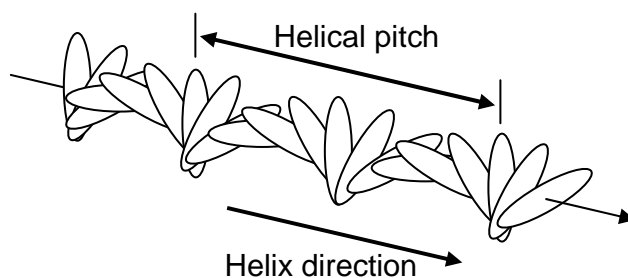
**FIG. 2.2.** Twist of the molecule in N* phase (left-handed twist).

Chiral Smectic C Phase

The *ferroelectric* (or more appropriate *helielectric*) SmC* phase can be obtained either by mixing chiral molecules with achiral molecules in the SmC phase, or by

synthesizing of a molecule with a chiral part including in the molecular structure. Molecules form a helicoidal structure similarly characterized by helical pitch and its sign. A *spontaneous polarization Ps* lying on the smectic layer plane is exhibited in the SmC* phase. The finding of *Ps* has been deduced from symmetry considerations.[2] The magnitude of the spontaneous polarization, the magnitude and the sign of the pitch can be controlled by mixing two or more chiral smectic compounds.

In the SmC* phase, the molecules also tilt with respect to the layer normal while the helix axis is along the layer normal. Notably, the director slowly rotates around the smectic cone progressively from layer to layer, preserving a constant *azimuthal angle φ* within a single layer (see Fig. 2.3). Since the helical pitch is in the order of micrometers, the director rotates around the full cone over several thousands smectic layers.
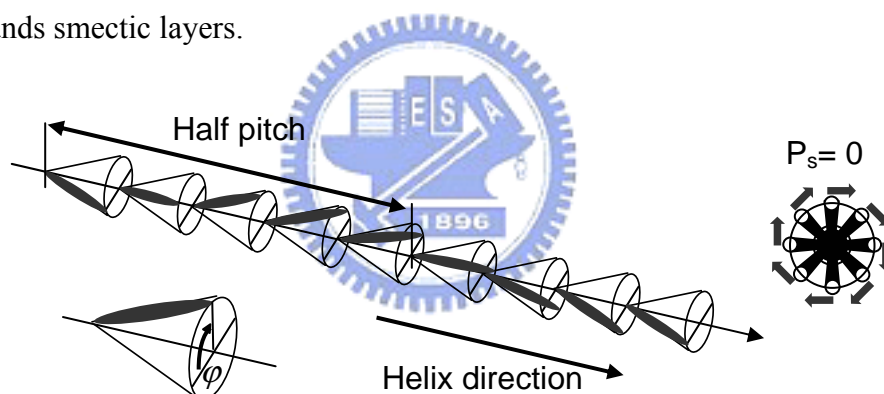
FIG. 2.3. Twist of the director in the SmC* phase. Due to the helical structure the polarization is canceled out on a macroscopic scale.

Since the polarization vector is always confined in the smectic layer plane, and perpendicular to the molecule, all possible directions of *Ps* are tangent to the basis of the smectic cone. In an undistorted field-free SmC* sample, where the helical structure is present, the spontaneous polarization will average to zero over one pitch, resulting in vanishing macroscopic polarization of the system (see Fig. 2.3). That is why the name helielectric is more appropriate, rather than ferroelectric. However, applying an electric field perpendicular to the helix axis will couple the

polarization vector to the field direction and unwind the helix, thus the **Ps** can be reoriented to the direction of applied field.

2.1.3 Basic Optics of a Liquid Crystal Thin Film

The essential properties of a liquid crystal are the optical, electric, and magnetic anisotropy. Optical anisotropy means that the index of refraction of the material depends on the direction of light polarization. The LC exhibits optical uniaxial symmetry (like N or SmA) with two principal refractive indices n_o and n_e. The ordinary refractive index n_o is for light with electric field polarization perpendicular to the director and the extraordinary refractive index n_e is for light with electric field polarization parallel to the director. The *birefringence* (or optical anisotropy) is defined as $\Delta n = n_e - n_o$. If $\Delta n > 0$, the LC is said to be optically positive whereas if $\Delta n < 0$, the LC is said to be optically negative. The *biaxial* materials (like SmC) exhibiting two optic axes can be characterized by three principal refractive indices: n_1, n_2 and n_3. The difference $\delta n = n_2 - n_1$ is called *optical biaxiality*. Since the biaxiality of liquid crystals is very small ($n_1 \approx n_2$), and can be neglected in most cases.[13]

A light beam entering the LC layer is split into two components: the *ordinary* and *extraordinary ray* owing to the presence of n_o and n_e. Both rays propagate through the birefringent medium at different velocities, leading to a phase difference Λ at the output of a uniformly aligned liquid crystal layer. The phase difference is defined by:

$$\Lambda = \frac{2\pi}{\lambda} \Delta n \cdot d \tag{2.1}$$

where λ is the wavelength of light in vacuum and d is the distance across the homogeneous LC layer (for normal incidence this is equal to the cell gap).

The optical transmission through a LC layer can be determined easily by using the Jones matrix method. Assume the LC layer is inserted between a pair of crossed polarizers (see Fig. 2.4). The incident light is linearly polarized by the

polarizer P, say with a polarization direction along the x axis, then being converted to elliptical polarized light by the birefrigent LC medium. Since the analyzer A is oriented at 90° with respect to the polarizer (i.e., along the y axis), only a fraction of the elliptical polarized light is able to pass through the analyzer. If the angle between the polarizer and the optic axis of the LC medium is α, then the transmitted beam for this case can be written as follows:

$$E = \begin{pmatrix} 0 & 0 \\ 0 & 1 \end{pmatrix} \begin{pmatrix} \cos\alpha & -\sin\alpha \\ \sin\alpha & \cos\alpha \end{pmatrix} \begin{pmatrix} e^{\frac{-i\Lambda}{2}} & 0 \\ 0 & e^{\frac{i\Lambda}{2}} \end{pmatrix} \begin{pmatrix} \cos\alpha & \sin\alpha \\ -\sin\alpha & \cos\alpha \end{pmatrix} \begin{pmatrix} 1 & 0 \\ 0 & 0 \end{pmatrix} E_0 \qquad (2.2)$$

where E_0 is the electric vector of the input linearly polarized beam, E is the electric vector of the output beam from the analyzer, and Λ is the phase difference induced by the LC layer. The transmitted intensity is therefore given by:

$$I = I_0 \sin^2 2\alpha \sin^2 \frac{\Lambda}{2} \qquad (2.3)$$

where I_0 is the intensity of the linearly polarized light, and $I = E^\dagger \cdot E$ where the dagger indicates the Hermitian conjugate. The setup shown in Fig. 2.4 is also the typical method widely used to measure the electro-optical response of a LC sample.
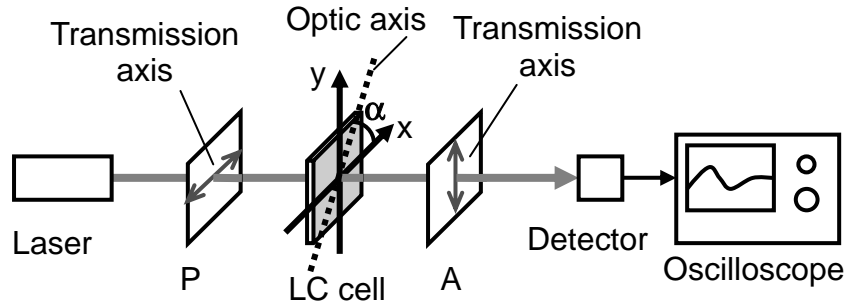
FIG. 2.4. A typical setup for measuring the transmission intensity of a LC cell.

The 2×2 Jones matrix method is a simple and efficient approach to study the propagation of plane wave with arbitrary polarization states through a multi-layer optical structures. However, in the Jones matrix method, the reflections and the

interference effect of light are neglected. The exact solution can be derived by 4×4 propagation matrix approaches. The 4×4 matrix methods, accounting for the reflection and interference effects when light beam passes through each layer, acquire intensive computations.

2.2 Liquid Crystal Display Technologies and Nematic Liquid Crystal Twisted Pi-Cell

Flat panel displays (FPDs) are increasingly important in information electronics products. Compared with the cathode ray tube (CRT) used in traditional televisions, FPDs are thin, lightweight, and power efficient devices that can present images with high quality performance. As a result, FPDs represent a large and rapidly growing industry worldwide, and are expanding into an increasingly diverse set of systems. Although in the field of FPD technologies, many different display technologies coexist with different levels of maturity, Liquid Crystal Displays (LCDs) have already achieved a significant market impact, which are the most important applications of the LC materials.

2.2.1 LCD Technology Today

LCDs are used everywhere. The applications of small scale LCDs include portable devices, such as mobile phones, digital cameras, portable DVD players, camcorders, handheld games, digital viewfinders, pictures viewers, price indicators and many others, which even did not exist a few years ago. And there appears to be no end to the applications requiring small sized displays. In the area of large screens (Active Matrix AM or Thin Film Transistor TFT technology), liquid crystals fit into all branches including video and TV applications along with high resolution laptop screens and desktop monitors.

Nowadays several competing technologies for large display format are

emerging. Among them *Active Matrix Liquid Crystal Displays* (AMLCDs) is probably the most promising one. AMLCD combines advantages – high resolution and good image quality, along with slim form and energy efficiency. The panels provide geometrically perfect, distortion-free images, focused homogenously over the entire screen. Inherent perfect flatness, lightness and low power requirements make it the most serious competitor to the CRT technology. In spite of many advantages, limited viewing angle, relatively slow response time and limited contrast are still the issues of the LCD displays.

Today's TFT-LCD market is essentially dominated by the *nematic technology*. Mainly two types of panels significantly penetrated the market: TN-LCD (Twisted Nematic) characterized by high contrast ratio and IPS-LCD (In Plane Switching) characterized by enhanced viewing angle. Recently a new configuration VAN-LCD (Vertically Aligned Nematics) is proposed combining both advantages at once. The nematic technology is well established and fits well into today's demands. Future displays, however, based on new device concepts, have much higher requirements, in which nematic materials may not be appropriate, especially in the issue of speed in particular.

In addition to nematics, *smectic liquid crystals* play a special role in LCDs due to the intrinsic fast response in the microsecond range. It means that the pixel speed is easily 1000 times faster than for nematics. Manufacturing smectic based devices is very challenging since it requires a laterally homogeneous inter-substrate spacing of less than 2 micrometers. Although smectics look promising from a material point of view, unreliable production, limited operating temperature range, gray level generation, and lower contrast are still unsolved issues. However, the technical developments highly rely on the further understanding of the alignment and reorientation dynamics of the smectic liquid crystals, which is the main subject of this thesis.
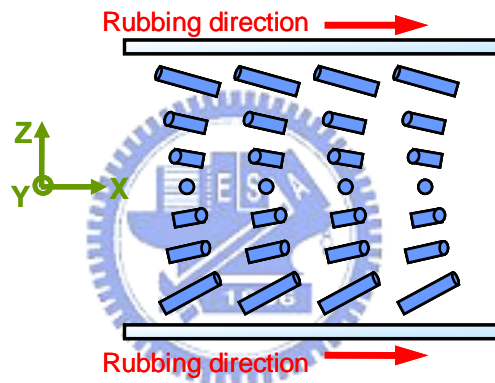
2.2.2 Nematic Twisted Pi-Cell

Twisted-nematic (TN) liquid crystal cells have been widely used in active matrix liquid crystal display (AMLCD) technology. Unfortunately in the TN mode, slow response and angular dependence of the image quality degrade the device performance. To overcome these drawbacks, the pi-cell[14] or optical compensated birefringence (OCB) LCD[15] has been proposed. However, the bend configuration in both pi-cell and OCB device is unstable at low driving field. In these devices, a more stable splay configuration appears first,[16] and a long warm-up period is needed to transform the LC device from the splay state to the bend state. This becomes problematic in multiplexed display applications, where the conversion of the inter-pixel LC molecules from the splay to the bend configuration is accompanied with disclination generation.[14,16] The display quality is thereby degraded. Two methods have been proposed for solving the problem. The first is to add a small fraction of polymeric chains into LC films to stabilize the bend configuration. Unfortunately, this approach produces hysteresis in the optical transmittance and decreases the optical quality with light scattering from the index mismatch between the liquid crystal and polymer. The second method adopts a high pretilt angle in the LC film. Although the stability of the bend configuration indeed improves with high pretilt angle, the device response time increases.

Recently a twisted nematic LC pi-cell structure is proposed by S. H. Chen *et al.* in 1999.[1] The twisted pi-cell exhibits a stable bend configuration by employing a N* phase LC. Here the N* phase LC is formed by doping the chiral material into the nematic LC. The rise and decay times of the optical response are shown to be 6 ms and 1.6 ms, respectively. Figure 2.5 is the structure of a typical LC cell which mainly consists of the bounding plates (ITO coated glass substrates), alignment layers and liquid crystals. The schematic diagram of a twisted pi-cell from the side view is shown in Fig. 2.6. The directors in the twisted pi-cell are twist from $\phi = 0°$ at the bottom plate to $\phi = -180°$ at the top plate. Although the switching process in

a twisted pi-cell has been investigated by optical transmission measurements and theoretical simulations,[1] the molecular alignment with varying field strength has not yet been explored experimentally.
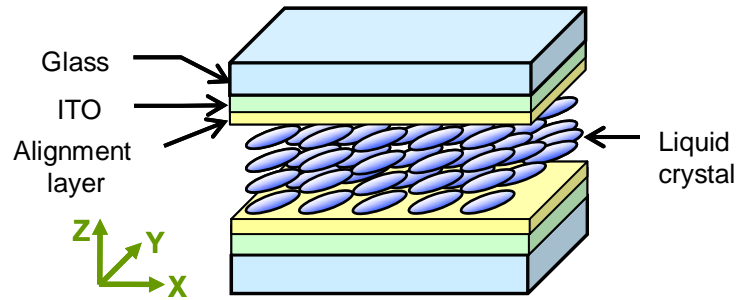
FIG. 2.5. Structure of a liquid crystal cell.


FIG. 2.6. A typical nematic twisted pi-cell.

2.3 Surface Stabilized Ferroelectric Liquid Crystals

In 1980, Noel A. Clark and Sven T. Lagerwall described a LC structure with a ferroelectric character of the SmC* phase: the Surface-Stabilized Ferroelectric Liquid Crystal (SSFLC) structure.[3] In principle, the bulk state of SmC* is not truly ferroelectric, because its macroscopic polarization is zero and does not yield different states with different polarization direction. However, when the helical symmetry, characterized by the bulk, is broken by surface interaction, macroscopic domains appear with a nonzero polarization which can point in two opposite directions. This is not only interesting from a point of view of material physics, but

immediately leads to an application potential with a new bistable electro-optic effect. The discovery of SSFLC initiated intense basic and applied research in this field.
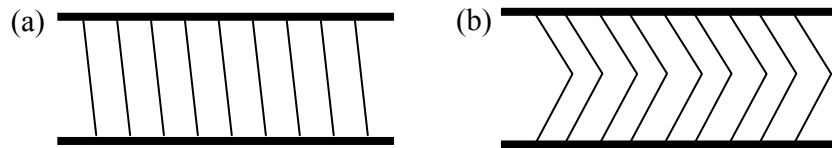
2.3.1 The SSFLC Structure

The SSFLC[3] exploits the geometry and surface interactions to unwind the helix, which requires a very thin gap in the cell, slightly smaller than the helical pitch. Generally the cell gaps are of the order of couples micrometers. Figure 2.7 shows a simplified SSFLC geometry. Here, the FLC is sandwiched between two bounding plates and the smectic layers are normal to the plates. The boundary conditions on the surface of the plates align *n* to lie on the plane. The boundary-induced preferred orientation, and the constraint of FLC which demands *n* on the tilt cone, produce two possible orientations of *n* at the intersections of the tilt cone with the surface of the bounding plates. The spontaneous polarization *Ps*, being normal to the surface, can then adopt only *up* or *down* orientation. This leads to the appearance of spontaneous domains of uniform polarization, which renders this structure to be ferroelectric. Ideally, the *n* orientations should be symmetric with equal minimum free energy and, thus, shall be equally stable. By applying electric fields of different polarity, the orientation of the director *n* can be switched between these two states.
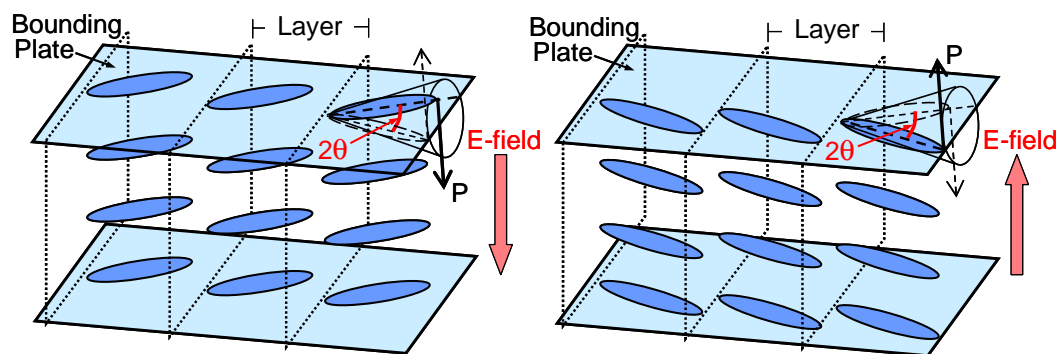
FIG. 2.7. The basic geometry of an SSFLC cell structure applied with external electric fields.

The cell structure is commonly called *bookshelf geometry*, named due to that the layers are ordered as books on a shelf. Typically, they are not strictly perpendicular to the surfaces, but more or less tilted (Fig. 2.8(a)). The bookshelf geometry can be used as a simple model. Another general structure is the *chevron structure*, in which the internal layers are folded (Fig. 2.8(b)). In the upright bookshelf geometry the desired molecular tilt angle θ (see Fig. 2.7) is 22.5°. The rotation of *n* is then 2θ = 45° and, consequently, the polarization direction of the light passing through the device can be rotated by 90°.


FIG. 2.8. Schematics of (a) a bookshelf structure with inclined layers and (b) a chevron structure.

2.3.2 Polar Switching

The SSFLC structure can be switched between two stable states by application of a voltage pulse of suitable duration. In contrast to the case of nematic liquid crystals, the threshold is here defined by the pulse area, rather than the amplitude alone, and the polarity of the pulse decides the switching direction. When the field is removed, the FLC relaxes to one of the stable states imposed by the interaction with aligning layers.

To briefly describe the electro-optical effects in the SSFLC cell, a simplified model is introduced. All layers are assumed to be inclined at an angle δ to the bounding plate. The simplified model simply considers the optical behavior for an optical beam propagation perpendicular to the bounding plate (Fig. 2.9).

$$\phi = 0$$
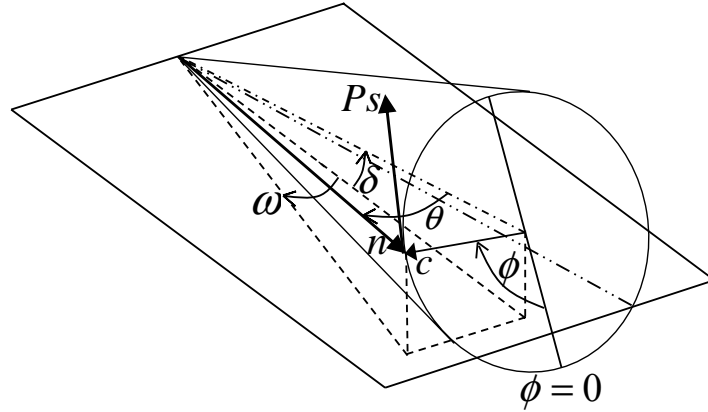
FIG. 2.9. Simplified model of the C* cone at the surface boundary in a cell with smectic layers tilted at angle δ. Rotation of the director **n** around the cone is described by the azimuthal angle ϕ ($\phi = 0$ at the bottom of the cone). ω is the angle between the projection of the cone axis on the cell surface and the corresponding projection of the director.

If the director is uniform, then the light transmission $I(t)$ through a cell between crossed polarizers with an input polarizer pointing to a direction of $22.5°$ (i.e., $\pi/8$) with respect to the cone axis, can be described by :[17]

$$I(t) = \frac{1 + \sin 4\omega(t)}{2} \sin^2 \frac{\pi \Delta n d}{\lambda} \tag{2.4}$$

where the angle ω between the projection of the cone axis on the cell surface and the corresponding projection of the director **n** is related to θ, δ and the instant angle $\phi(t)$ of director around the cone by

$$\tan \omega(t) = \frac{\sin \phi(t) \tan \theta}{\cos \delta - \sin \delta \tan \theta \cos \phi(t)} \tag{2.5}$$

If the thickness d of the cell is chosen to satisfy the half-wave condition ($\Delta n d = \lambda/2$) then the transmission becomes:

$$I(t) = \frac{1 + \sin 4\omega(t)}{2} \tag{2.6}$$

There are four main torques acting on the switching FLC director, which include a ferroelectric toque Γ_F driving the director to move around the cone, a dielectric torque Γ_D pushing the director to an extreme position, a viscous torque

Γ_V resisting the movement and an elastic torque Γ_K acting towards one of the relaxed states. In a dynamic equilibrium, the instant angle $\phi(t)$ must satisfied the balance condition of these torques by

$$\Gamma_F + \Gamma_D + \Gamma_V + \Gamma_K = 0 \tag{2.7}$$

where the four torques can be expressed by following.[18,19]

$$\Gamma_F = EP_S \cos\delta \cos\phi \tag{2.8}$$

The dielectric torque has to include the biaxial properties of the dielectric tensor. This can be expressed using an effective dielectric parameter:

$$\varepsilon_\Delta = \partial\varepsilon - \Delta\varepsilon \sin^2\theta \tag{2.9}$$

where $\partial\varepsilon = \varepsilon_2 - \varepsilon_1, \Delta\varepsilon = \varepsilon_3 - \varepsilon_1$ and $\varepsilon_1, \varepsilon_2, \varepsilon_3$ is the diagonal terms of the dielectric tensor. In agreement with Jones et al.,[20] the dielectric torque is then described by

$$\Gamma_D = \frac{\varepsilon_0 \varepsilon_\Delta}{2} E^2 \cos^2\delta \left(\sin 2\phi - 2\cos\phi_v \sin\phi\right) \tag{2.10}$$

and becomes zero at the limiting angular values + and − (with an infinite applied voltage), which can be calculated from:

$$\cos\phi_v = -\frac{\Delta\varepsilon \sin 2\theta \tan\delta}{2\varepsilon_\Delta}. \tag{2.11}$$

In a bookshelf geometry or if $\Delta\varepsilon = 0$, the angle $\phi_V = \pi/2$. In the typical case of chevron cells and negative dielectric anisotropy, is smaller than π/2.

The viscous torque counteracts the change of ϕ and is expressed by

$$\Gamma_V = -\eta_c \frac{d\phi}{dt}, \tag{2.12}$$

where η_c is the rotational viscosity depending on the tilt according to

$$\eta_c = \eta \sin^2\theta. \tag{2.13}$$

Finally, the elastic torque is approximated by[18]

$$\Gamma_K = \frac{\eta_c}{t_R} \left(\sin 2\phi - 2\cos\phi_0 \sin\phi\right) \tag{2.14}$$

where t_R is an observable relaxation time. The elastic torque Γ_K becomes zero at the two stable angular positions $\pm\phi_0$ which, by definition, are the two relaxed (or memorized) states.

2.4 Molecular Reorientation Dynamics of Liquid Crystal Thin Films

The generation of liquid crystal phases is limited by both steric and polarity considerations, meaning that the liquid crystal phases can only exhibit by materials with specific molecular structures. To be suitable for an application, a material must satisfy the following basic requirements. The molecular structure is required to generate a desired liquid crystal phase at a specific temperature with a suitable temperature range. In addition the material also needs to possess a suitable combination of physical properties for that application.[11] Therefore an understanding on the structure-property relationships of liquid crystals is highly crucial.

Typically the rod-shaped liquid crystal materials can be simplified by a model consisting of a rigid central core and flexible tails.[21] The rigid core provides the steric interaction of rigid rods that stabilizes orientationally ordered phases. The flexible tails suppress crystallization. In electro-optic applications the LC molecules are driven by an applied external field and reorient during the switching dynamics. As a result, the induced variation of the optical anisotropy modulates the polarization states of the incident light. This electro-optic effect is essentially attributed to the averaged behaviors of all liquid crystal molecules, while the different molecular fragments play various roles in the reorientation process. Therefore, the further understanding about how the inter-molecular and intra-molecular motions influence the macroscopic electro-optical switching dynamics is highly required due to the interest from LC physics and technology.

However, the investigation of molecular conformations and arrangements in equilibrium and during molecular transient motion is still a virtually unexplored area, but potentially a very rich subject, since it offers a new window into the molecular-level behavior influencing macroscopic dynamic properties.[21-22] In this thesis, we study the field-induced molecular reorientation dynamics of liquid crystal thin films, including a nematic liquid crystal twisted pi-cell and surface stabilized ferroelectric liquid crystals (SSFLC), with submolecular specificity.

From the view point of realistic application, the fast electro-optic response of LCDs is a basic requirement to fulfill the video-rate conditions. By introducing a twisted structure to the conventional pi-cell, the response time is significantly reduced from more than 10 ms to about 2 ms, which is unachievable by other geometries of nematic LCD. Although the response time of a twisted pi-cell can be push to a millisecond scale, it reaches the speed limit of nematic LC. To break this limitation, SSFLCs are one of the most promising liquid crystal materials which exhibit a response time of microseconds.

The vibrational spectroscopy is employed to investigate the field-induced molecular reorientation dynamics of a nematic twisted pi-cell and SSFLC, owing to the high sensitivity on reflecting the small changes in the bonding and geometrical arrangement of molecular segments. In this study, we applied the infrared absorption and Raman scattering techniques to investigate the LC thin films. The IR and Raman spectroscopies can provide valuable information about the conformation and orientational motions of individual segments of LC molecules. To clearly reveal the submolecular arrangements, polarization-dependent measurements can be employed in the IR absorption and Raman spectroscopy. For example, in systems of uniaxial symmetry (i.e., nematic and smectic A), simple dichroic ratio measurements can yield information that IR absorption can provide. However, upon a transition to lower symmetry, such as that of the smectic C* phase, dichroism changes may arise from either (or both) director reorientation or symmetry changes. Unraveling these phenomena requires measurement of absorbance over a continuous range of polarizer orientations and

analysis of the resulting pattern of absorbance vs. polarization orientation.[23-26] Similar to the polarized infrared spectroscopy, the polarized Raman spectroscopy also can yield this kind of information.

Chapter 3

Time-Resolved

Vibrational Spectroscopy

In this chapter, we first briefly review the basic principles of vibrational spectroscopy, including the IR absorption spectroscopy and the Raman spectroscopy. Since the transient behavior of a LC molecular system during a dynamic switching process is of main interest in this study, a time-resolving scheme with a microsecond time resolution has to be developed for the vibrational spectroscopic study. Over past years, many different approaches have been proposed to perform the time-resolving spectroscopic measurements. Asynchronous time-resolved IR spectroscopy is employed in this study due to the advantage of plug-compatibility. The principle of asynchronous time-resolved spectroscopy is illustrated in Sec. 3.2. Unfortunately, as the time-resolved scheme is combined with a polarization-dependent measurement, the data acquisition becomes extreme time consuming. To significantly improve the data-taking efficiency of time-resolved IR spectra, we constructed multichannel time-resolving system based on the asynchronous time-resolving method, which is described in Sec. 3.3. The complex and large amounts of IR spectra obtained from the time-resolved polarized FTIR require an efficient data analysis methodology to reveal the dynamic processes of LC molecular fragments. Two-dimensional (2D) correlation spectroscopy is a technique where the spectral intensity is plotted as a function of two independent spectral variables. By spreading peaks along the second spectral dimension; one can gain advantage to sort out complex or overlapped spectral features that normally cannot be detected via the conventional spectroscopy. Owing to the enhancement of spectral resolution and sensitivity of

perturbation-induced spectral variation, the 2D correlation analysis is introduced into the IR spectroscopic studies of the SSFLCs. The intramolecular correlated motions in a steady dc field and during a field-induced reorientation process thus can be explored in detail. The theoretical consideration of 2D correlation spectroscopy is briefly reviewed in Sec. 3.4.

3.1 Infrared and Raman Spectroscopy

Molecules are comprised of atoms. The atoms in a molecule, which are connected by chemical bonds, can exhibit periodic *vibrational* motions.[27] All atomic motions in a molecule relative to each other are a superposition of so-called *normal vibrations*, in which all atoms are vibrating with the same phase and *normal frequency*. Polyatomic molecules with n atoms possess $3n-6$ (or $3n-5$) vibrations and each vibration is called a *normal mode*. The vibration amplitudes can be described by a *normal coordinate*. The normal modes of molecules can be probed with a variety of *vibrational spectroscopies*. The spectra yielded depend on the atomic masses, geometrical arrangement of atoms, and the strength of their chemical bonds. Molecular aggregates behave like 'super molecules' in which the vibrations of the individual components are coupled.

Infrared and Raman spectrometers are the most important tools for observing vibrational spectra. Molecular vibrations may be *active* or *forbidden* in the infrared or Raman spectrum, depending on the vibrational natures of the molecular symmetries. The infrared and Raman spectra of two molecules may be different if the molecules have different constitutions, configurations, conformation and locate in different environments. Therefore materials can be identified by their infrared and Raman spectra with fingerprinting capability.

The Infrared Spectrum

According to quantum mechanics the molecule can take up a quantized energy $h\nu_s$ to reach the first vibrational excited state. Light quanta in the infrared region with a wavelength λ of 2.5 to 1000 μm possess energies of $h\nu = hc\tilde{\nu}$ with $\tilde{\nu} = 4000$ to 10 cm^{-1}. A molecule irradiated with a continuous spectrum of infrared radiation may absorb light quanta having the energy $h\nu_s$, therefore the spectrum of the remaining radiation shows an absorption band at the frequency ν_s. Figure 3.1(a) demonstrates this process.

Infrared spectra are usually obtained by measuring the transmittance of the sample with a continuous distribution of light quanta. A molecule with n atoms possesses $k=3n-6$ normal vibrations. These vibrations may only absorb infrared radiation if they modulate the molecular dipole moment μ_K:

$$\mu_k = \mu_0 + \left(\frac{\partial\mu}{\partial q_k}\right)_0 q_k + \frac{1}{2}\left(\frac{\partial^2\mu}{\partial q_k^2}\right)_0 q_k^2 + \cdots \tag{3.1}$$

with the kth normal coordinate $q_k = q_k^0 \cdot \cos(2\pi\nu_k t + \varphi_k)$.

Interaction of infrared radiation with a vibrating molecule is only possible if the electric field of the radiation oscillates with the same frequency as does the molecular dipole moment. A vibration is *infrared active* only if the molecular dipole moment can be modulated by the normal vibration, i.e.,

$$\left(\frac{\partial\mu}{\partial q}\right)_0 \neq 0. \tag{3.2}$$

If the condition in Eq. (3.2) is fulfilled by symmetry, then the vibrations are said to be *allowed* or *active* in the infrared spectrum, otherwise they are said to be *forbidden* or *inactive*.
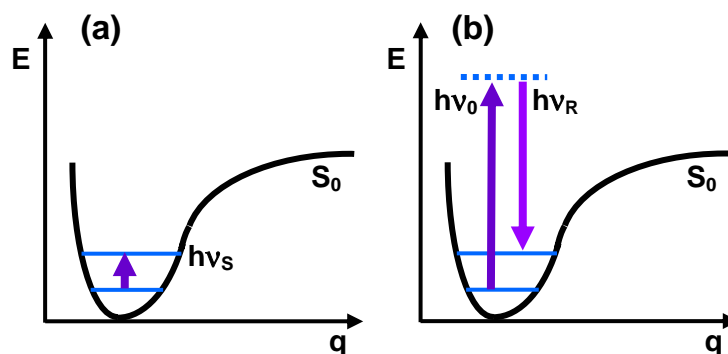
FIG. 3.1. The excitation of a vibrational state in the electronic ground state S_0 by (a) infrared absorption, and (b) Raman scattering.

The Raman Spectrum

The vibration may also be excited by a different mechanism, such as by inelastic scattering of light quanta of higher energy, the so-called Raman effect, illustrated in Fig. 3.1(b). In this case, the molecules are irradiated with monochromatic radiation in the ultraviolet, visible or near infrared spectral region, whose quanta have the energy $h\nu_0$. During an inelastic impact of light quantum with a molecule, vibrational energy $h\nu_s$ can be exchanged. Thus, the scattered light quanta have a lower or higher energy $h\nu_R$ with

$$h\nu_R = h\nu_0 \mp h\nu_s,\qquad (3.3)$$

where $h\nu_s$ is the vibrational energy. The energy quanta $h\nu_R$ give rise to a Raman spectrum. At the same time, the exciting light quanta are also elastically scattered, which is the Rayleigh scattering. In this case, the scattered quanta have the same energy as the exciting radiation.

When a molecule is exposed to an electric field, electrons and nuclei are forced to move in opposite directions. A dipole moment is induced which is proportional to the electric field strength and the molecular polarizability α. The polarizability depends on the flexibility of the electrons and nuclei in the molecule. The electric field induced dipole moment μ' can be described by its components:

$$\mu_x^{'} = \alpha_{xx}E_x + \alpha_{xy}E_y + \alpha_{xz}E_z$$
$$\mu_y^{'} = \alpha_{yx}E_x + \alpha_{yy}E_y + \alpha_{yz}E_z \quad . \tag{3.4}$$
$$\mu_z^{'} = \alpha_{zx}E_x + \alpha_{zy}E_y + \alpha_{zz}E_z$$

This can be written as

$$\mu' = \alpha E \quad . \tag{3.5}$$

All α_{ij} are components of a tensor $\boldsymbol{\alpha}$, which projects the electric field $\boldsymbol{E}$, to produce another vector $\boldsymbol{\mu'}$, the induced dipole moment.

The modulation of the polarizability of a molecule by a vibration with the frequency ν_k can be described by

$$\alpha_k = \alpha_0 + \left(\frac{\partial \alpha}{\partial q_k}\right)_0 q_k^0 \cdot \cos 2\pi\nu_k t + \cdots . \tag{3.6}$$

As a consequence of irradiation, the magnitude of the electric field vector is modulated with the frequency ν_0, and the molecule shows an induced dipole moment:

$$\mu_k^{'} = \alpha_0 E_0 \cos 2\pi\nu_0 t + \left(\frac{\partial \alpha}{\partial q_k}\right)_0 q_k^0 E_0 \cos 2\pi\nu_0 t \cdot \cos 2\pi\nu_k t . \tag{3.7}$$

This is equivalent to

$$\mu_k^{'} = \alpha_0 E_0 \cos 2\pi\nu_0 t + \frac{1}{2}\left(\frac{\partial \alpha}{\partial q_k}\right)_0 q_k^0 E_0 \left[\cos 2\pi(\nu_0 - \nu_k)t + \cos 2\pi(\nu_0 + \nu_k)t\right]. \tag{3.8}$$

The first term describes the Rayleigh scattering, the second term represents the Stokes Raman scattering and the third term the anti-Stokes Raman scattering. A molecular vibration can only be observed in the Raman spectrum if there is a modulation of the molecular polarizability by the vibration,

$$\left(\frac{\partial \alpha}{\partial q}\right)_0 \neq 0 . \tag{3.9}$$

If the condition in Eq. (3.9) is fulfilled by symmetry, then the vibrations are *allowed* or *active* in the Raman spectrum, otherwise they are *forbidden* or *inactive*.
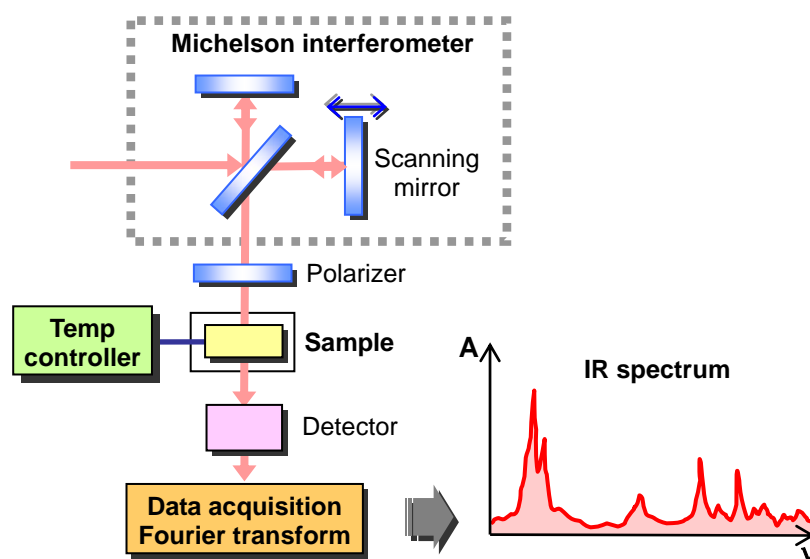
3.2 Time-Resolved FTIR

Fourier transform spectroscopy (FTS) has clear advantages over many other techniques (Fig. 3.2) to yield broad spectral range with high resolution.[28] In addition to excellent frequency resolution, FTS allows accurate determination of absolute frequencies without the need for calibration. The high throughput and multiplex advantage of FTS give signal-to-noise (S/N) improvements over dispersive spectroscopic techniques. Recent developments incorporating time resolution into the FTS techniques have created a powerful and versatile spectroscopic method for characterizing dynamic process.[29] Time-resolved Fourier transform spectroscopy (TRFTS) has been used to investigate photo-dissociation reactions, bimolecular reaction, condensed phase systems such as polymer, and surface studies for monitoring the kinetics of adsorption, desorption, diffusion, and ordering.[30-33]

The main benefit of all TRFTS experiments is that spectral and temporal information can be gained from the same measurement.[34-38] Today's TRFTS is implemented mainly in two fundamental ways:[39]

(i) The most common setup is the coupling of a step-scan interferometer with a laser/transient digitizer or grated integrator system. Spectral and time resolutions achieve values of 0.25 cm^{-1} and <100 ns, respectively.[40] Using TRFTS based on step-scan interferometer spectral resolution of 0.05 cm^{-1} and time resolution of 100ps have been reached.[41,42]

(ii) Another scheme is the synchronization of a continuous-scan Fourier transform interferometer with a laser and a transient digitizer or a gated integrator. With TRFTS based on continuous-scan interferometer spectral resolution of 0.2 cm^{-1} and time resolution of 1 μsec have been reported.[43]

Both methods of course benefit from the advantages of TRFTS.

FIG. 3.2. Schematic of FTIR system.

Over the last decade various kinds of time-resolved infrared spectrometers have been developed and applied to a variety of research fields.[44-46] In 1992 Masutani *et al.*[5] proposed a time-resolving method for a conventional Fourier-transform infrared (FTIR) spectrometer, named as *asynchronous time-resolving system*. The most important characteristic of the asynchronous time-resolving system is that the method does not require synchronization between the timing for time resolving and that for the sampling of the analog-to-digital (A/D) converter. The main advantage of this method is that the signal-processing assembly for time-resolving measurements can be attached to any kinds of commercial continuous-scan FTIR spectrometers with a temporal resolution limited only by either the IR pulse duration or the detector response time. Therefore, asynchronous time-resolved FTIR spectroscopy has been extensively employed to investigate repetitive fast phenomena such as the field-induced reorientation dynamics of a number of FLCs.[23,26,47-52]

3.2.1 Principle of Asynchronous Time-Resolved FTIR Spectroscopy

The principle of asynchronous time-resolved FTIR spectroscopy is qualitatively described as following. Detail formulation description can be referred to the original paper of Masutani *et al.* in 1992.[5] Here we focus the discussion on a single channel asynchronous time-resolved system.[5]
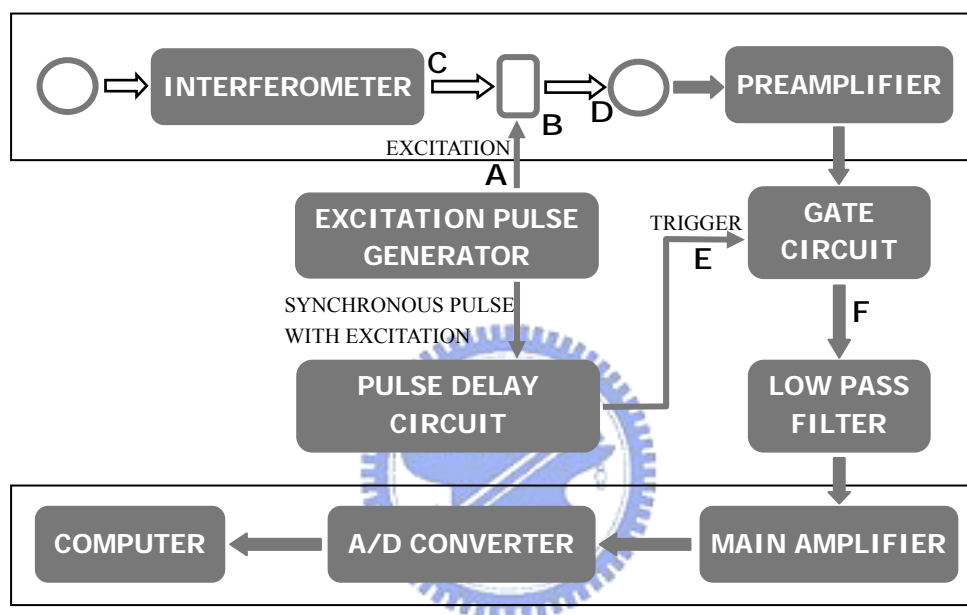
FIG. 3.3. A typical setup for the asynchronous time-resolved measurement. The signal-processing assembly for time-resolved measurements is shown in the middle, while the units constituting a conventional FTIR spectrometer are depicted in doubly lined boxes at the top and bottom.

Figure 3.3 shows a typical setup for the asynchronous time-resolved measurement.[5] To carry out the time-resolving measurement, a signal-processing assembly (shown in the middle part of Fig. 3.3) is attached to a conventional continuous-scan FTIR system. The required components in the assembly include a pulse generator, a pulse delay circuit, a gate circuit, and a low-pass filter. The main feature of this method is the use of a low-pass filter placed between the gate circuit and the A/D converter. Assuming that when excitation pulses are generated with a time period τ to stimulate the sample, the sample shows a periodic response

induced by the excitation. The transmittance spectrum after the sample can be described by

$$T(\bar{v},t) = T_0(\bar{v}) + \Delta T(\bar{v},t) * \text{III}_\tau(t), \qquad (3.10)$$

where $T_0(\bar{v})$ is the component unchanged by the excitation, and $T(\bar{v},t)$ is that changed by the excitation. Variables $\bar{v}$ and t are, respectively, the spectral wave number and time variable relating to the excitation. $\text{III}_\tau(t)$ is Dirac delta comb used to represent the repetitive operation with a period of τ. An interferogram generated from the interferometer will be modulated by the excitations. The modulated interferogram $F(x,t)$ can be expressed as

$$F(x,t) = \int_{-\infty}^{+\infty} T(\bar{v},t) B(\bar{v}) \cos 2\pi x \bar{v} \, d\bar{v}$$
$$= F_0 + \int_{-\infty}^{+\infty} \{ T(\bar{v},t) * \text{III}_\tau(t) \} \cdot B(\bar{v}) \cos 2\pi x \bar{v} \, d\bar{v} \quad \text{with} \qquad (3.11)$$
$$F_0(x) = \int_{-\infty}^{+\infty} T_0(\bar{v}) B(\bar{v}) \cos 2\pi x \bar{v} \, d\bar{v},$$

where $F_0(x)$ is the constant component of the interferogram unchanged by the excitation, and $B(\bar{v})$ is the spectrum of the light source. The trigger pulses generated from delay circuit are delayed from the leading excitation pulses by a time interval $\Delta\tau$. The modulated interferogram signals arriving at the gate circuit are converted into a discrete interferogram time-resolved at delay time $\Delta\tau$ from the excitation, which is set by the trigger pulse. The resulting discrete interferogram is given as

$$F(x,t) = \text{III}_\tau(t - \Delta\tau) \cdot [F_0(x) + \int_{-\infty}^{+\infty} \{ \Delta T(\bar{v},t) * \text{III}_\tau(t) \} \cdot B(\bar{v}) \cos 2\pi x \bar{v} \, d\bar{v}]$$
$$= \text{III}_\tau(t - \Delta\tau) \cdot \int_{-\infty}^{+\infty} T(\bar{v},\Delta t) B(\bar{v}) \cos 2\pi x \bar{v} \, d\bar{v}, \qquad (3.12)$$

where $\mathrm{III}_\tau(t-\Delta\tau)$ is used to express the gating by the trigger pulse. A time-resolved continuous interferogram for delay time $\Delta\tau$ can be obtained from the low-pass filter by removing the high-frequency component. The output from low-pass filter can therefore be expressed as

$$F(x,\Delta\tau)=(1/\tau)\int_{-\infty}^{+\infty}T(\overline{V},\Delta t)B(\overline{V})\cos 2\pi x\overline{V}\,d\overline{V} \qquad (3.13)$$

for the time-resolved continuous interferogram at delay time $\Delta\tau$ from the excitation. The time-resolved interferogram for delay time $\Delta\tau$ is sampled by the A/D converter at its own sampling period τ_0, and is acquired by computer. Inverse Fourier transformation of the digitized interferogram finally gives a time-resolved spectrum at time delay $\Delta\tau$ from the excitation.

To illustrate the asynchronous time-resolved approach more clearly, a simulated curve was generated step by step and the result was shown in Fig. 3.4. Figures 3.4(A) to 3.4(F) are correspondent signals of processes A to F in Fig. 3.3. Figure 3.4(A) shows the excitation pulses with period τ and Fig. 3.4(B) is the responses of the sample to the excitations in A. We assume that a broad band infrared light source generates an interferogram x(t) without excitations (see Fig. 3.4(C)), in which t represents time. The infrared light source covers a spectrum from 1000 to 4000 cm^{-1}. The original interferogram x(t) is modulated by the excited sample, in which the modulation frequency is the same frequency as the excitation pulses. The modulated interferogram $x_m(t)$ (full line) is plotted in Fig. 3.4(D) with the original interferogram x(t) (broken curve) for comparison. Set the trigger pulses (full line in Fig. 3.4(E)) delayed from the preceding excitation pulses (broken line) by a constant time interval $\Delta\tau$, therefore the frequency of the trigger pulses is the same as that of the excitation pulses. The gate circuit controlled by the trigger signal acquires the data of the modulated interferogram $x_m(t)$ and a discrete time-resolved interferogram can be obtained. Figure 3.4(F) shows the discrete interferogram $x_d(t)$ (full line) which is time-resolved at delay time $\Delta\tau$ from the excitation and the corresponding modulated interferogram $x_m(t)$ (broken curve).
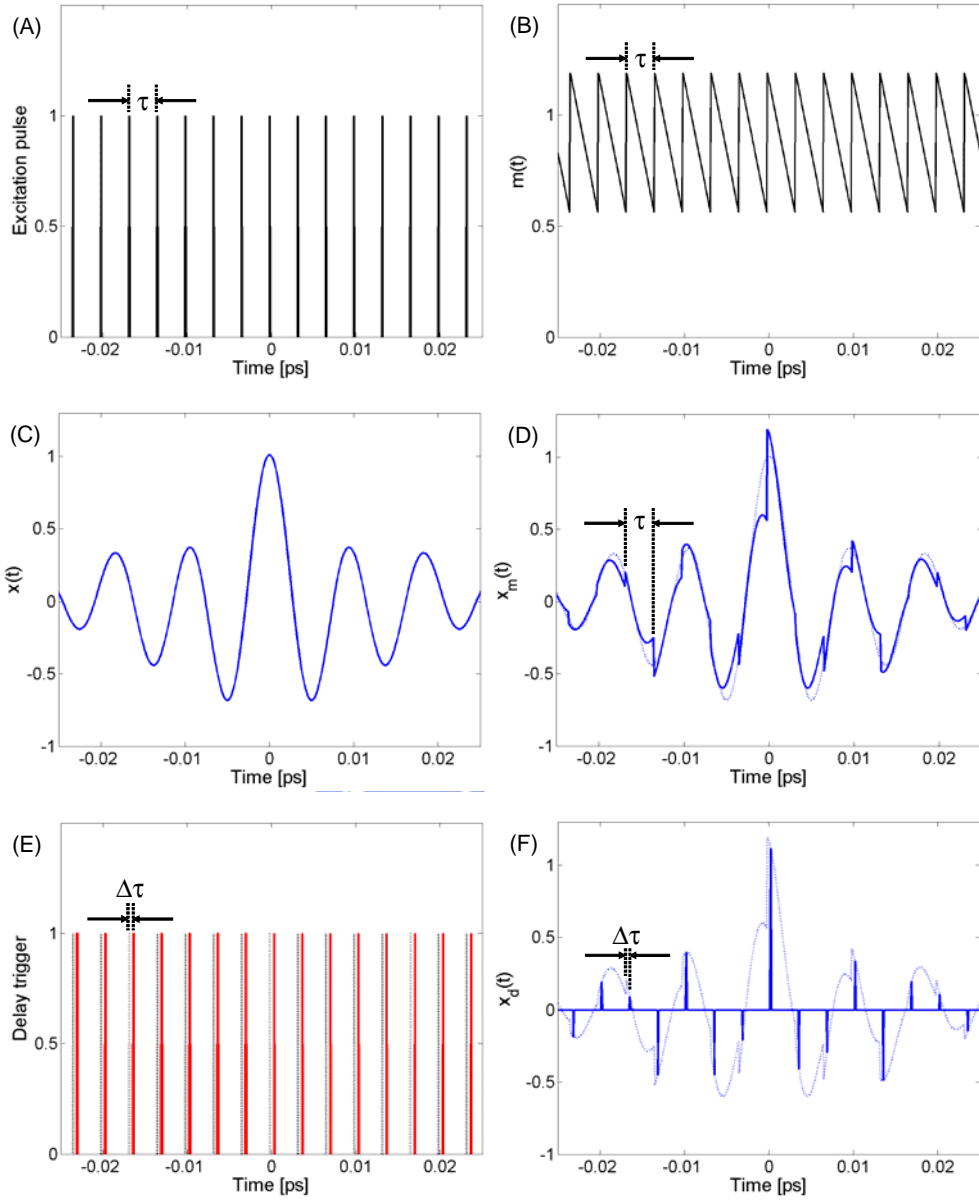
FIG. 3.4. The shapes of the signals in processes A-F in Fig. 3.3. (A) Excitation pulses with period τ; (B) responses of the sample to the excitations in A; (C) an interferogram without excitations; (D) an interferogram modulated by the excitations in A (full curve) and the unmodulated interferogram (broken curve, the same one as in C); (E) trigger pulses (full line) delayed from the preceding excitation pulses (broken line) by a time interval $\Delta\tau$; (F) a discrete interferogram time-resolved at delay time $\Delta\tau$ from the excitation (full line) and the corresponding modulated interferogram (broken curve, the same one as in D).

By using the low-pass filter, the discrete time-resolved interferogram can be

transformed into a continuous transient interferogram at delay time $\Delta\tau$. The role of the low-pass filter is demonstrated in Fig. 3.5.[5] The discrete interferogram $x_d(t)$ sampled by the gate circuit at delay time $\Delta\tau$ is Fourier transformed and the corresponding spectrum is obtained. Figure 3.5(A) shows the corresponding spectrum $\widetilde{X}_d(f)$, where f represents the frequency. The spectrum $\widetilde{X}_d(f)$ consists of the original components and higher-frequency components. The original components have a maximum cut-off frequency f_M. The higher-frequency components appear at positions determined by integral times of the sampling frequency $1/\tau$. To check the discrete interferogram, inversed Fourier transform is applied to $\widetilde{X}_d(f)$ and the resulting discrete interferogram $FFT^{-1}[\widetilde{X}_d(f)]$ is shown in Fig. 3.5(B), which exactly reproduces the discrete interferogram $x_d(t)$, indicating that the Fourier transform and inversed Fourier transform used here work properly. When the discrete interferogram $x_d(t)$ is passed through a low-pass filter with an appropriate cutoff frequency f_C, the high-frequency components are eliminated. For the spectrum $\widetilde{X}_d(f)$, the cut-off frequency f_C of the low-pass filter is set to be 5000 cm^{-1}. The output spectrum $\widetilde{X}_{d,filtered}(f)$ from the low-pass filter is shown in Fig. 3.5(C). Finally, inversed Fourier transform of $\widetilde{X}_{d,filtered}(f)$ gives the continuous transient interferogram $FFT^{-1}[\widetilde{X}_{d,filtered}(f)]$ at time delay $\Delta\tau$ (see Fig. 3.5(D)). To check the correctness of the generated time-resolved interferogram, the real transient spectrum and interferogram at delay time $\Delta\tau$ are calculated. The real continuous transient spectrum $\widetilde{X}_{m,\tau}(f)$ shown in Fig. 3.5(E) is identical to the spectrum $\widetilde{X}_{d,filtered}(f)$ with a constant multiplier. Figure 3.5(F) shows the calculated real transient interferogram $x_{m,\tau}(t)$ (full line) and the analog interferogram output $FFT^{-1}[\widetilde{X}_{d,filtered}(f)]$ (dotted line) from the low-pass filter, in which the curves are totally overlapped without any distortion. Consequently, the time-resolved continuous interferogram can be obtained correctly from the

asynchronous scheme with gated circuit and low-pass filter.[5]
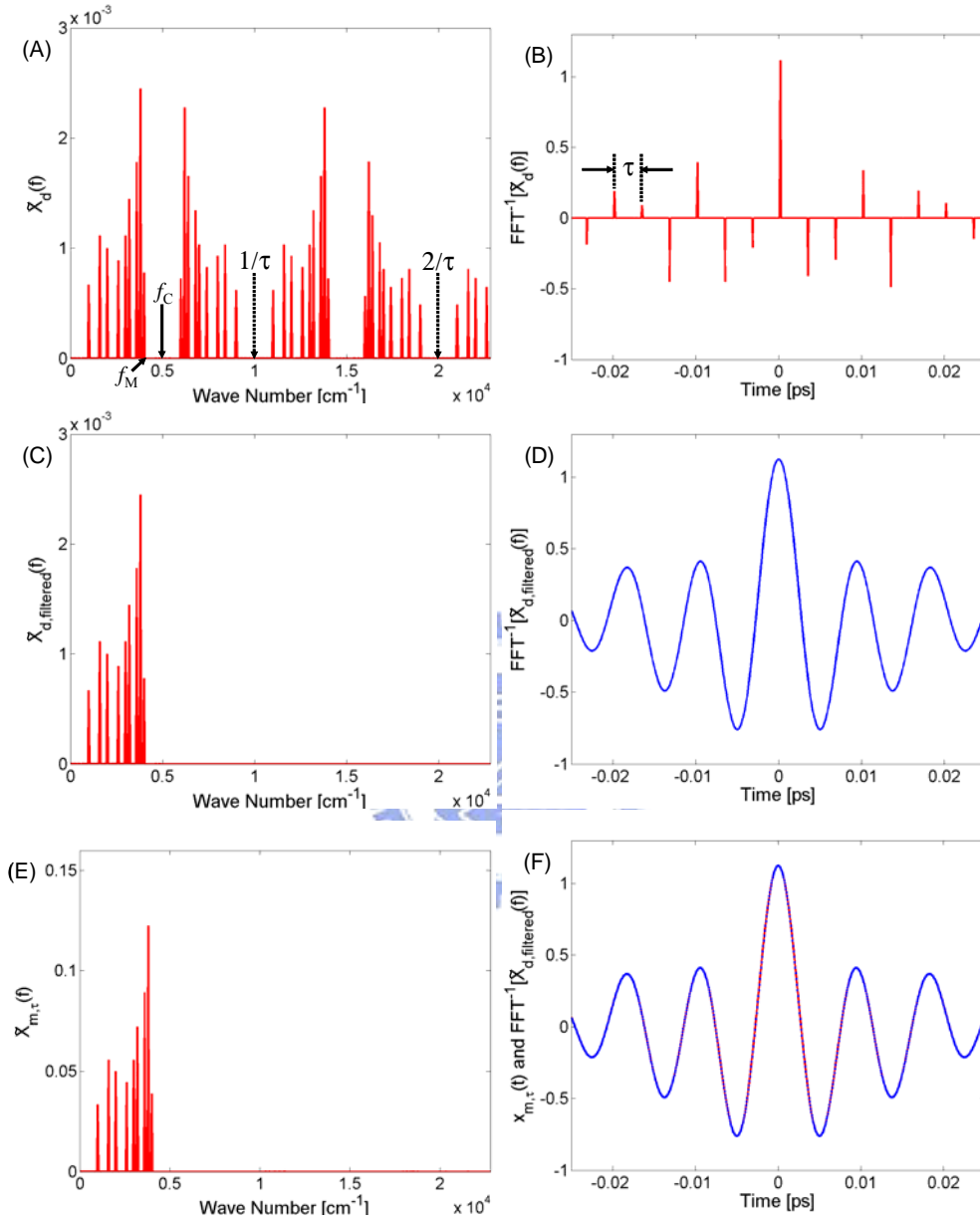
FIG. 3.5. Role of the low-pass filter. (A) The spectrum corresponding to the discrete interferogram of Fig. 3.4(F) with a sampling time interval τ; (B) The inverse Fourier transform of (A) gives the same discrete interferogram; (C) frequency response of the low-pass filter with a cut-off frequency f_C; (D) the inverse Fourier transform of the spectrum from the low-pass filter deduced the analog transient interferogram at delay time $\Delta\tau$; (E) the spectrum obtained by Fourier transform of the real transient interferogram at delay time $\Delta\tau$; (F) the transient interferogram obtained from low pass filter (broken line) exactly reproduced the real transient interferogram at delay time $\Delta\tau$ (full line).

3.3 Multichannel Time-Resolved FTIR

As the time-resolved scheme is combined with a polarization-dependent measurement, the data acquisition takes a significant amount of time. To substantially reduce the data-taking time of the time-resolved FTIR, we further construct a multichannel asynchronous time-resolving system based on the module demonstrated by Matsutani *et al.* in 1999.[6] In addition, simultaneous time-resolved data-taking by the multichannel system also improves the reliability of the data and decrease the possible stimulus-induced damage of the sample.

The advantage of the multichannel time-resolving scheme on the remarkable improvement in data-taking efficiency can be illustrated with Fig. 3.6, which shows the data acquisition procedure in a time-resolved angular-dependent measurement. Assuming that the measurement includes two parameters, the azimuthal-angle scan of the IR polarization and time, there are in total i*j sets of data to be acquired, which ranges from Φ_1 to Φ_i for azimuthal angle and t_1 to t_j for delay time. The left part of the figure shows the data acquiring sequence of the conventional single channel system, the bold numbers in the grid represent the order of the data-taking. The measurement is carried out block by block and starts from the set (Φ_1, t_1), then (Φ_2, t_1), (Φ_3, t_1), ..…, and so on. To complete the whole measurement, it spends a fairly long period of time. However, the data acquiring sequence in the time-resolved multichannel system with j temporal channels, which is shown in the right part of the figure, starts from the column (Φ_1, t_1 to t_j), to (Φ_i, t_1 to t_j). Since the multichannel time-resolved system can acquires all the time-resolved sequence at one time, so the data-acquisition only takes 1/j times the duration of the conventional single channel time-resolved measurement.
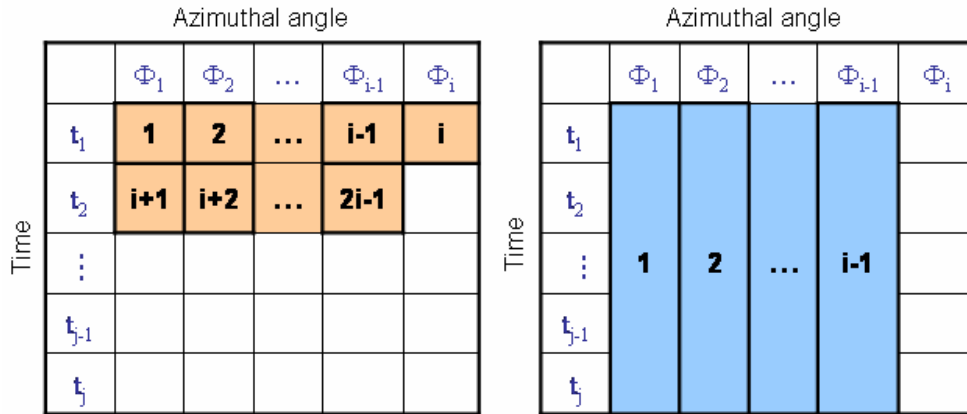
FIG. 3.6. The schematics of the data acquisition procedure of the time-resolved measurement. Left part shows the data acquiring sequence of the conventional single channel system and right part shows the data acquiring sequence in the multichannel time-resolved system.

3.3.1 Descriptions of the Multichannel Time-Resolved System

Figure 3.7 shows the schematic diagram of our multichannel system. The time-resolved system has 32 time-resolving units, each consisting of a sample-and-hold circuit and a low-pass filter. In this system, time resolving is performed by setting each sampling-hold circuit at a different time delay. The sample is excited by repetitive stimuli at constant intervals, which is independent of the sampling timing of the FTIR spectrometer. The repetitive stimuli in our case are the excitation electric pulses, which also serve as the common trigger of the various time delays. The sample excitations result in transient transmission differences, and thus the continuous interferogram is modulated at very high frequency due to the repetitive excitation of the sample. The low-pass filters eliminate high-frequency components from the discrete time-resolved signals generated by the sampling-hold circuit, thus converting discrete signals to analog signals. The obtained analog signals are processed by the A/D converter at the same sampling rate as that of the FTIR spectrometer. Therefore the trigger signal for the data sampling does not relate to the gate timing of the sampling-hold for time resolution.[5]
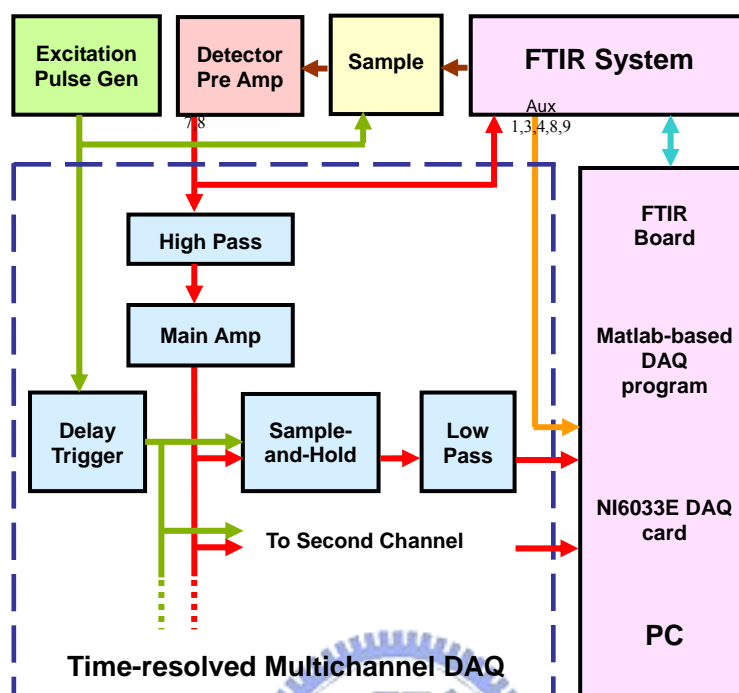
FIG. 3.7. Schematic diagram of a multichannel FTIR system.

In principle, the time-resolved multichannel asynchronous scan system could have a time resolution of 50 ns, which depends on the specification of the delay circuit. However, the system is particularly limited by the rising time of the IR detector employed. Although repetitive stimuli do not depend on the sampling timing of the FTIR spectrometer, they are restricted on the basis of the sampling theorem, i.e., the repetitive rate of sample excitation must be no less than twice the highest Fourier frequency in the spectral range.[5]

It should be also noted that in this study the time-resolved multichannel asynchronous scan system applies only to time-resolving measurement with a continuous-wave IR probe. For the pump/probe scheme with a pulsed IR probe, the temporal resolution of the asynchronous scan technique can be as short as the pulse duration of the probing pulse used.

3.3.2 Accuracy Test of the Multichannel Time-Resolved System

The accuracy test for this system was carried out by measuring the IR source spectrum in air. For this purpose, the time-resolved multichannel asynchronous scan system was attached to an FTIR spectrometer (MIR8000, ORIEL) equipped with a HgCdTe detector. The infrared spectrum of light source in air was measured with the above-mentioned spectrometer in the conventional data-collection mode. At the same time, we can acquire another spectrum using the interferogram obtained by a specific channel of the multichannel asynchronous scan system. The IR interferogram in air measured by the first channel of the multichannel system was obtained from single scan, whereas the one by conventional FTIR system was acquired with 64 co-add from multi-scans. The resulting interferograms are shown in Fig. 3.8. These interferograms are very close to each other over the entire spectral range, indicating that the multichannel system does not produce any distortion and introduce extra noise to the acquired spectra. Same tests were applied to check every channel of the 32 channels and similar results were obtained, confirming that the multichannel system can yield accurate time-resolved results.

To further verify the precision of the multichannel system, the interferograms in air were measured by the 32 channels with single scan. The experimental data are presented in Fig. 3.9. A high similarity between the interferograms obtained from various channels was observed, indicating that the multichannel time-resolving system are quite stable and the precision of measurements are preserved.
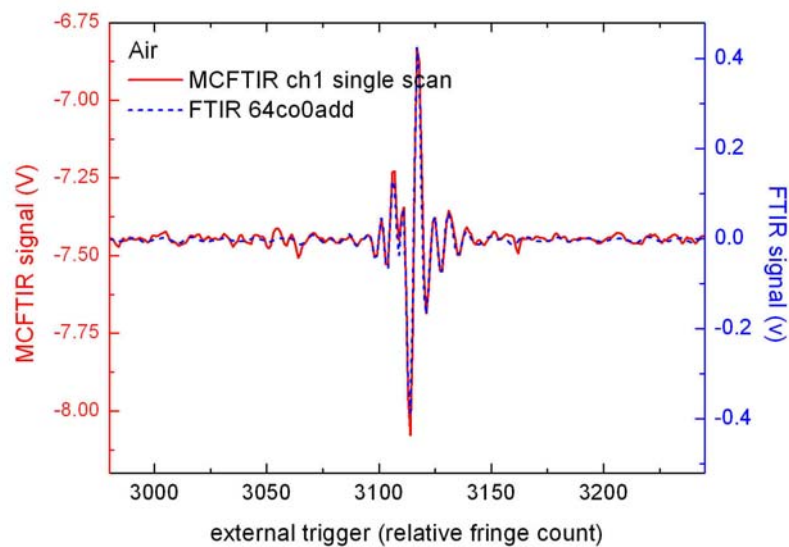
FIG. 3.8. Comparison of the interferograms of air obtained from the MCFTIR system and the conventional FTIR spectrometer.
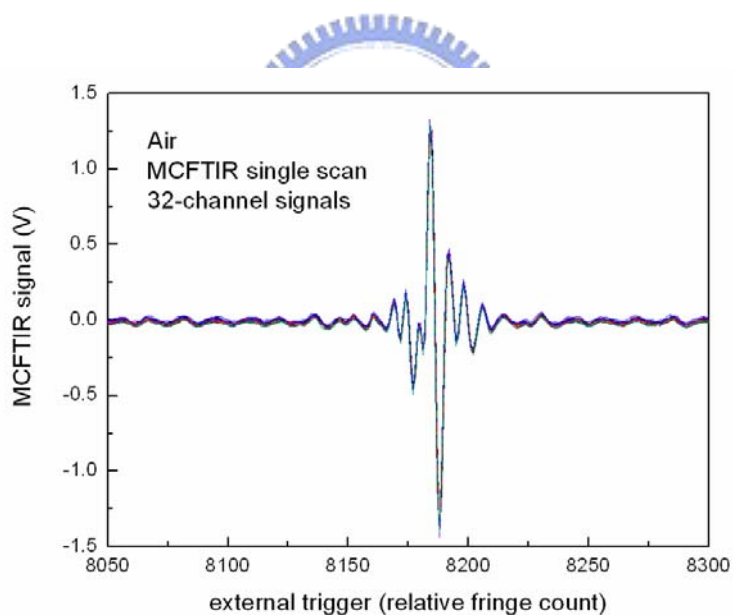
FIG. 3.9. The interferograms of air obtained from the 32 channels in the multichannel time-resolved system.

3.4 Two-Dimensional Correlation Spectroscopy

Two-dimensional (*2D*) *correlation spectroscopy* is a technique where the spectral intensity is plotted as a function of two independent spectral variables. 2D *spectroscopy* was originally proposed in the field of NMR spectroscopy around 1970s.[53-56] By spreading peaks along the second spectral dimension; one can gain the following advantages, which is not easily obtainable from the conventional one-dimensional spectrum.[57] i) Simplifying the complex spectra comprising many overlapped peaks, and enhancing the spectral resolution by spreading peaks over the second dimension; ii) Establishing unambiguous assignments through correlation analysis of bands; iii) Probing the specific order of the spectral intensity changes occurring during the measurement or by controlling the parameters that can affect the spectrum; iv) Investigating the correlation between bands in two different spectra (hetero spectral correlation), for example, correlation between an infrared (IR) band and a near-IR (NIR) band, or the same data but different ranges of controlling parameters.

2D correlation spectroscopy in optical spectroscopy was first proposed by Noda as 2D IR spectroscopy in 1986.[57-59] A simple cross-correlation analysis was applied to analyze sinusoidally varying dynamic IR signals to yield a set of 2D IR correlation spectra. This method is unlike the time-domain double Fourier transform (FT) methods used in multiple-pulse excitation 2D NMR.[57-59] This 2D correlation approach has one major shortcoming; the time-dependent behavior (i.e., waveform) of dynamic spectral intensity variation must be a simple sinusoid to effectively employ the original data analysis scheme.[57-59] To overcome this limitation, Noda[60] expanded the concept of 2D correlation spectroscopy to include more general forms of spectra intensity variation application in 1993 (generalized 2D correlation spectroscopy). The mathematical procedure to yield 2D correlation spectra from sinusoidally varying time-dependent spectral signals was modified to allow handle arbitrary time-dependent forms. The type of spectral signals that can

be analyzed by the newly proposed 2D correlation method is extremely broad, covering IR, NIR, Raman, X-ray, fluorescence, and many more. The introduction of the generalized 2D correlation spectroscopy has expanded greatly applications of 2D correlation analysis in various branches of science and technology.

Nowadays, 2D correlation spectroscopy has been used in analytical chemistry, physical chemistry, material sciences, biological and medical sciences, food and agricultural sciences, and chemical industries.[7,61-68] It is applied to analyze of inter and intramolecular interactions, chemical reactions, electrochemistry, adsorption, photochemistry, hydration, denaturation, special distributions, rheology, clinical diagnosis, and many more.
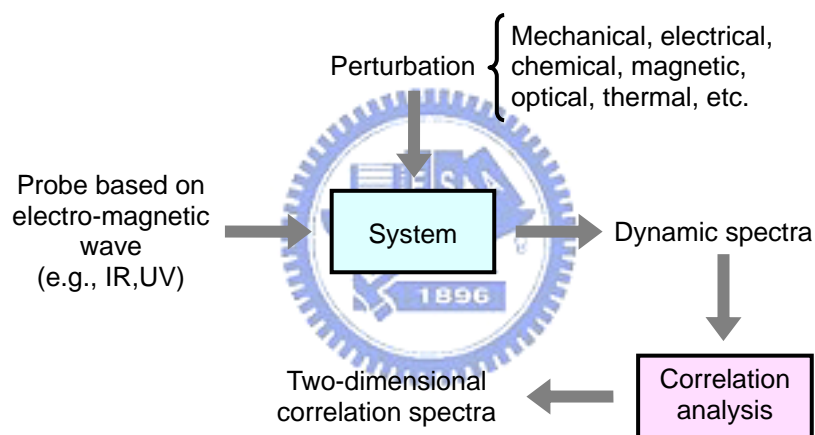
FIG. 3.10. General scheme for obtaining 2D correlation spectra.

Figure 3.10 shows the basic scheme for a 2D correlation spectroscopy with an external perturbation.[59-60] In the formal scheme of generalized correlation, a selected electro-magnetic probe is used to study the system of interesting. Characteristic interaction between the probe and constituents of the system are then analyzed in the form of a spectrum to reveal the detail information of the system. An additional perturbation applied during the spectroscopic measurement is utilized to stimulate the system of interesting. One can use numerous types of physical stimuli, such as mechanical, electrical, chemical, and magnetic and waveforms, such as sinusoid, pulse, ramp, as the perturbations. The response of the

system to the applied perturbation often exhibits itself as characteristic variations in the optical spectrum, known as a *dynamic spectrum*. Based on the 2D correlation analysis, two kinds of correlation spectra, known as synchronous and asynchronous 2D spectra, are generated from the dynamic spectra.

3.4.1 Principle of Two-Dimensional Correlation Analysis

For a spectral intensity variation $y(v,t)$ observed is a function of a spectral variable v during an interval of some perturbing parameter t between T_{min} and T_{max}. Although the external variable t can be any measure of physical quantity such as time, temperature, pressure, concentration, etc., hereafter t will be referred to as time for convenience. The dynamic spectrum $\tilde{y}(v,t)$ is defined as

$$\tilde{y}(v,t) = \begin{cases} y(v,t) - \bar{y}(v) & T_{min} \leq t \leq T_{max} \\ 0 & \text{otherwise} \end{cases} \tag{3.14}$$

where $\bar{y}$ is the reference spectrum of the system. The selection of a reference spectrum is not strict, but in most cases one can set $\bar{y}(v)$ to be the averaged spectrum defined by the following equation.

$$\bar{y}(v) = \frac{1}{T} \int_{-T/2}^{T/2} y(v,t)\, dt \tag{3.15}$$

A different type of reference spectrum may be selected by choosing a spectrum obtained at some fixed reference point. It is also possible to set the reference spectrum to be zero.

A formal definition of the generalized 2D correlation spectrum $C(v_1,v_2)$ is given by

$$\begin{aligned} C(v_1,v_2) &= \langle \tilde{y}(v_1,t)\tilde{y}(v_2,t) \rangle_{T_{min} \leq t \leq T_{max}} \\ &= Syn(v_1,v_2) + iAsyn(v_1,v_2) \\ &= \frac{1}{\pi(T_{max} - T_{min})} \int_0^\infty \tilde{y}(v_1,\omega) \cdot \tilde{y}*(v_2,\omega)\, d\omega \end{aligned} \tag{3.16}$$

The term $\tilde{y}(v_1,\omega)$ is the forward Fourier transform of the spectral intensity

variations $\tilde{y}(\nu_1, t)$ observed at some spectral variable ν_1

$$\tilde{y}(\nu_1, \omega) = \int_{-\infty}^{\infty} \tilde{y}(\nu_1, t)\, e^{-i\omega t} dt$$

$$= \tilde{y}^{Re}(\nu_1, \omega) + i\tilde{y}^{Im}(\nu_1, \omega)$$

(3.17)

where $\tilde{y}^{Re}(\nu_1, \omega)$ and $\tilde{y}^{Im}(\nu_1, \omega)$ are, respectively, the real and the imaginary components of the Fourier transform.

The 2D correlation spectrum comprises two orthogonal components $Syn(\nu_1, \nu_2)$ and $Asyn(\nu_1, \nu_2)$, known, respectively, as the synchronous and asynchronous 2D correlation intensities.[60,69] They represent, respectively, the overall similarities and differences of the time-dependent behavior of spectral intensity variations measured at two distinct spectral variables, ν_1 and ν_2, during the observation period between T_{min} and T_{max}.

Equation (3.16) provides a functional comparison of intensity variation $\tilde{y}(\nu, t)$ at different spectral variables ν_1 and ν_2, which is performed within a fixed interval of the perturbing parameter $T_{min} \leq t \leq T_{max}$.
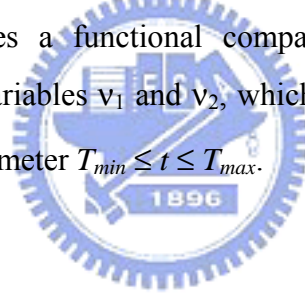
3.4.2 Properties of 2D Correlation Spectra

The intensity of a synchronous 2D correlation spectrum $Syn(\nu_1, \nu_2)$ represents the simultaneous or coincidental changes of spectral intensity variations measured at ν_1 and ν_2 during the interval $[T_{min}, T_{max}]$ of an externally applied perturbation t. Figure 3.11(a) is a schematic of a synchronous 2D correlation spectrum. A synchronous spectrum is symmetric with respect to a diagonal line corresponding to $\nu_1 = \nu_2$. The peaks located at diagonal are referred to as *auto-peaks*. Auto-peaks are identical mathematically to the autocorrelation function of spectrum intensity variations observed during an interval between T_{min} and T_{max}. The magnitude of an auto-peak intensity represents the overall extent of spectral intensity variation observed at the specific spectral variable ν during the interval between T_{min} and

T_{max}. Note that, auto-peak intensity is always positive. Any region of a spectrum, where shows a significant change in intensity under a given perturbation will exhibit a strong auto-peak, while those remaining near constant develop few or no auto-peak. Thus, an auto-peak represents that the overall susceptibility of the corresponding spectral region changes in spectral intensity as an external perturbation is applied to the system.
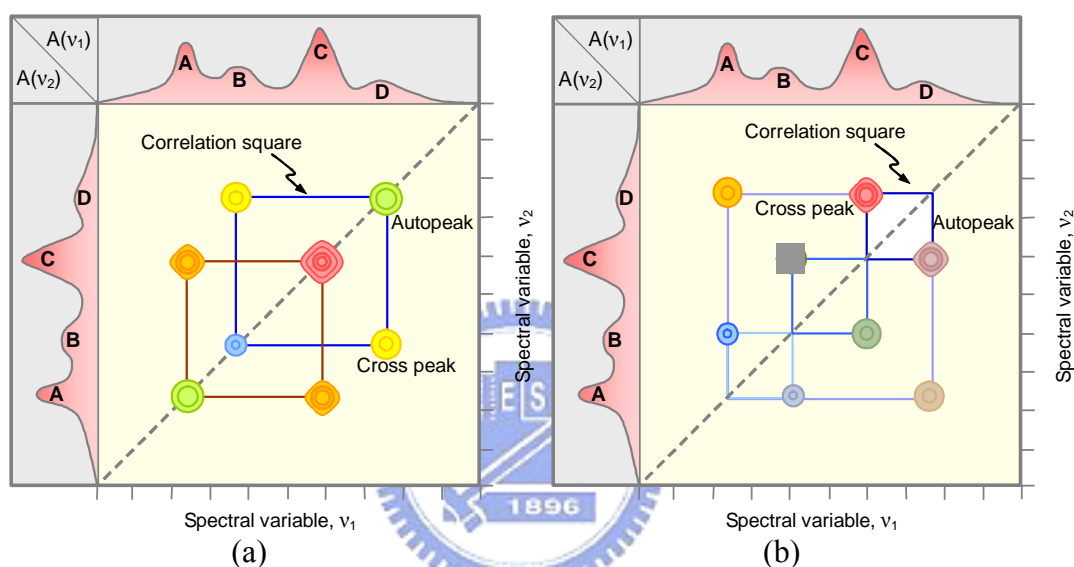
FIG. 3.11. Schematic contour map of (a) a synchronous 2D correlation spectrum, and (b) an asynchronous 2D correlation spectrum.

Cross-peaks located at the off-diagonal positions of a synchronous 2D spectrum represent simultaneous or coincidental changes of spectral intensities observed at two different spectral variable ν_1 and ν_2. The possible existence of a coupling between the spectral intensity variations could be revealed by a synchronous cross-peak. The sign of cross-peaks can be either positive or negative. If the spectral intensities corresponding to the cross-peak is either increasing or decreasing together, the sign of the cross-peaks is positive; otherwise, the sign of the cross-peak is negative.

The intensity of an asynchronous 2D correlation spectrum represents sequential, or successive, changes of spectral intensity measured at ν_1 and ν_2 (see

Fig. 3.11(b)). Unlike a synchronous spectrum, an asynchronous spectrum is antisymmetric. Typically the asynchronous 2D spectrum should have no auto-peaks, and has only of cross-peaks. An asynchronous cross-peak appears when the intensities of two spectral features changes out of phase (i.e., delayed or accelerated) with each other. This feature is especially useful in differentiating overlapped bands arising from spectral signals of different origins. Even if bands are located close to each other, as long as the signatures of spectral intensities are substantially different, asynchronous cross-peaks will develop. The signs of asynchronous cross-peaks can be either positive or negative. The sign of an asynchronous cross-peak become positive, if the intensity change at ν_1 occurs predominantly before ν_2 in the sequential order of t. It becomes negative, if the change occurs at ν_1 after ν_2. However, the sign is revered if $Syn(\nu_1, \nu_2) < 0$.

Chapter 4

Switching Dynamics

of Twisted Nematic

Liquid Crystal Pi-Cells

The twisted nematic LC pi-cell can exhibit a more rapid electro-optic response than other nematic LC cell. Although the switching process in a twisted pi-cell has been investigated by optical transmission measurement and theoretical simulation,[1] the molecular alignment with varying field strength has not yet been explored experimentally. Therefore, in this chapter, we applied vibrational spectroscopies to probe the molecular orientation, in order to utilize their 'fingerprinting' capability. The results of molecular alignment and reorientation in a twisted pi-cell with polarized Fourier transform infrared absorption (pFTIR) spectroscopy[22] and Raman spectroscopy[70] are reported in this chapter.

4.1 Experimental Procedures

Samples of twisted pi-cell were assembled with two ITO-coated CaF_2 plates. The substrates were coated with a 700~800Å thick RN1842 (from Nissan Co.) alignment layer and rubbed to yield a 2° pretilt angle for the LC molecules used. The cell gap was maintained at $d = 6$ μm with proper spacers. ZLI2293 liquid crystal (from Merck Co.), doped with 0.71 wt% S811 left handed chiral molecules, was used to fill the empty cell above the LC clearing temperature. The cell was then slowly cooled to 30 °C to produce a pitch of p = 15 μm and satisfy the condition d/p = 0.4.[16] The LC cells were then enclosed with UV-cured sealant.
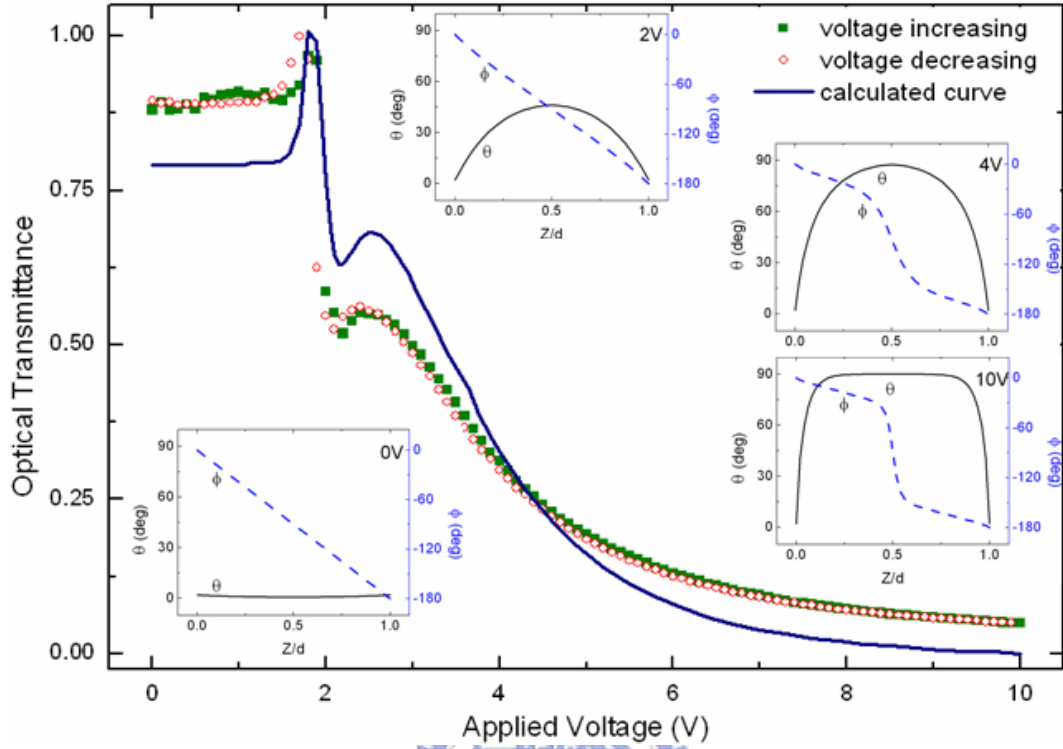
FIG. 4.1. Measured optical transmission of a twisted pi-cell as a function of applied voltage. The calculated *T-V* curve (solid curve) and the underlying director profiles (inset) at 0, 2, 4, and 10 V are included for comparison.

We first investigated the optical transmittance (T) versus voltage (V) by inserting the LC cell into a crossed polarizer-analyzer setup with a helium-neon laser at 632.8 nm as the light source. The rubbing direction of the cell substrates was rotated 45° from the transmission axis of the input polarizer. An electric field with voltage increasing from 0 to 10 V was first applied on the LC cell. The transmittances obtained are presented in Fig. 4.1 (filled squares). The LC cell was then stabilized at the high field for a brief period and then the voltage was decreased from 10 to 0 V. The resulting transmittances are shown with the open symbols. No hysteresis was observed, indicating that the underlying LC configuration is stable. To explore further, we performed a simulation on the LC cell with the elastic theory of continuum medium under varying voltage. The calculated optical transmission shown by the solid curve agrees reasonably well with experimental observation, indicating that the calculated LC profiles (presented

in the inset at 0, 2, 4 and 10 V) are precise in depicting the LC configuration.

FTIR spectra from 900 to 4000 cm^{-1} with 4 cm^{-1} resolution were recorded with an Oriel MIR8000 FTIR spectrometer equipped with a liquid nitrogen cooled MCT detector. A wire-grid polarizer on a rotation stage was used to control the polarization of the incident IR beam. The sample was excited with a 2 kHz bipolar square wave with varying voltage.

An experimental setup used to acquire transient Raman spectra from a LC cell during field-induced switching is depicted in Fig. 4.2. The incident laser beam with a wavelength of 523 nm was polarized along the rubbing direction of the pi-cell. The timing between the laser probing and the electrical driving field on the LC cell was controlled with a combination of function generator and digital delay generator. The Raman scattered photons were collected by a microscope objective lens and detected with a charge coupled device (CCD) camera through a spectrograph. The CCD was cooled to −20 °C with a thermoelectric cooler.
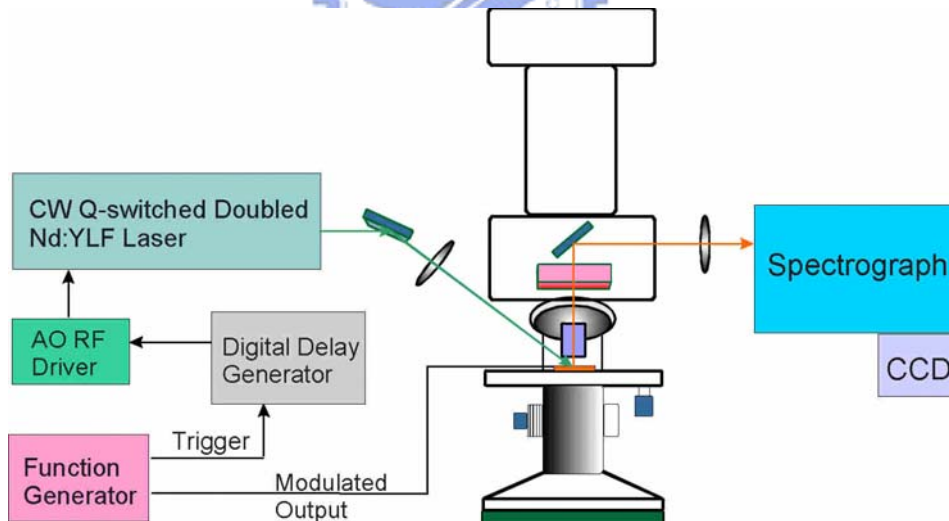

FIG. 4.2. Experimental set-up for acquiring transient Raman spectra from a LC cell during the field-induced switching process.

4.2. Results and Discussion

4.2.1. Polarized Fourier-Transform Infrared Absorption Spectroscopy of a Twisted LC Pi-Cell

A typical FTIR spectrum of a twisted LC pi-cell is presented in Fig. 4.3. The polarization of the incident infrared beam is oriented to the rubbing direction. The six peaks were found to lie at 1448, 1502, 1606, 2228, 2851, and 2924 cm^{-1}. The highest two peaks at 2851 and 2924 cm^{-1} are contributed from the symmetric (s-CH_2) and anti-symmetric (a-CH_2) stretches along the alkyl chain of the LC molecules. The peak at 2228 cm^{-1} can be attributed to C≡N stretch and the features at 1606 and 1502 cm^{-1} are mainly from the C=C stretch of the LC core. A combination of the C–C stretch and the C–H in-plane wag on the LC core leads to the 1448 cm^{-1} peak. The mode assignments are summarized in the Table 4.1, accompanied by the calculated normal mode vibrations of the cyano biphenyl core using a density functional theory package.[71]
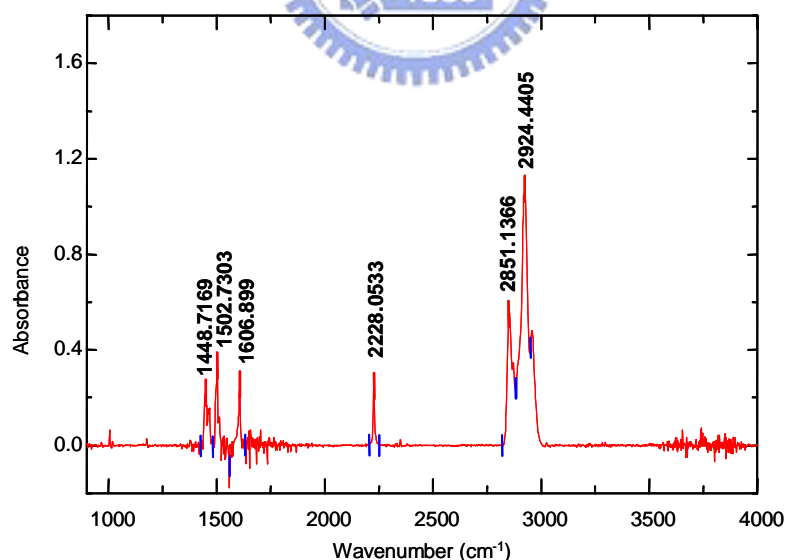

FIG. 4.3. Fourier-transform infrared absorption spectrum of a twisted pi-cell with an applied voltage of 0 V. The polarization of the incident infrared beam is oriented to the rubbing direction.

**Table 4.1.** Calculated and measured normal-mode frequencies of cyano biphenyl.
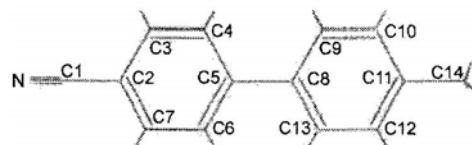
Normal modes	Vibration frequency/cm^{-1}		IR absorption	Symmetry
1. C=H stretch				
s-CH$_2$	2851 (IR)	2851 (Raman)		
a-CH$_2$	2924 (IR)			
f-CH$_3$		2937 (Raman)		
2. C1≡N stretch	2237 (calc.)		89.8	A_1
	2228 (IR)	2228 (Raman)		
3. Biphenyl C=C stretch	1605 (calc.)		46.3	A_1
	1606 (IR)	1606 (Raman)		
	1502 (IR)			
4. (a) biphenyl C–C+C–H in-plane wag	1446 (calc.)		29.5	A_1
	1448 (IR)			
(b) C5 – C8 stretch + C–H in-plane wag	1261 (calc.)		6.5	A_1
		1265 (Raman)		
		1240 (Raman)		
5. C(biphenyl)–H in-plane	1095 (calc.)		13.9	A_1
		1177 (Raman)		
6. Biphenyl in-plane angular distortion	985 (calc.)		4.2	A_1
		957 (Raman)		
	510 (calc.)		5.9	
7. C– H out-of-plane wag	507 (calc.)		9.9	B_1
	544 (calc.)		6.3	
	664 (calc.)		42.8	
	713 (calc.)	705 (Raman)	11.8	
	742 (calc.)		45.7	
	818 (calc.)	790 (Raman)	23.2	
		821 (Raman)		

In Fig. 4.4 the measured IR peak intensities are presented as a function of the azimuthal angle between the infrared polarization and the rubbing direction of the cell. The three major peaks from the LC core at 1502, 1606, and 2228 cm^{-1} exhibit very similar azimuthal patterns. Their peak amplitudes and dichroic ratios also display significant dependence on the applied voltage.
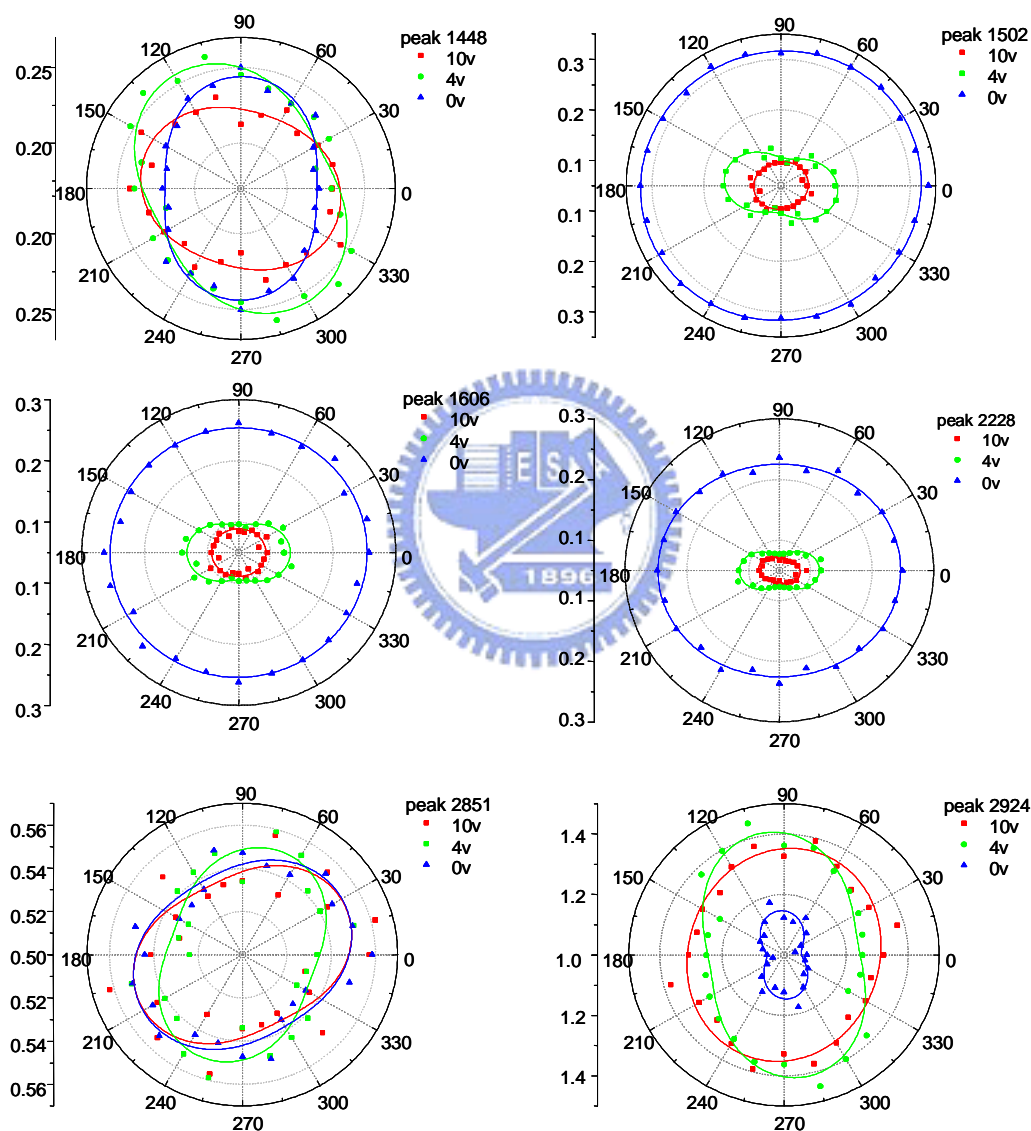
FIG. 4.4. Azimuthal patterns of the infrared absorption peaks of a twisted pi-cell with varying applied voltages. The azimuthal angle denotes the angle between the infrared polarization and the rubbing direction of the cell.
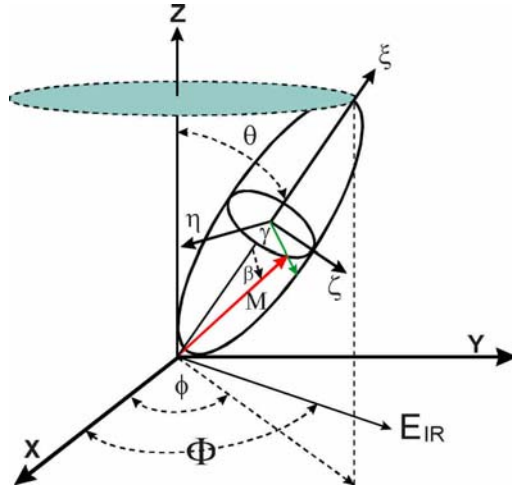
FIG. 4.5. Schematic diagram showing the relationship between the molecular frame ($\xi\eta\zeta$) and the laboratory coordinates system (XYZ).

To investigate the molecular alignment further, we performed simulations with various LC alignment models. Note that the infrared absorption by an optical anisotropic film can be properly described with a 2nd rank absorbance tensor[72]

$$A(\Phi) = \frac{N\pi}{3c} \int [\mu_g^{(K)} \cdot \hat{E}]^2 f(\Omega) \, d\Omega \qquad (4.1)$$

where Φ denotes the angle between the incident infrared polarization and the X-axis of the laboratory coordinates system (see Fig. 4.5), and $f(\Omega)$ is the orientational distribution of the dipole moment derivative. With a normal incidence on the XY-plane, the integrated IR absorbance can be expressed as

$$A(\Phi) = \frac{1}{3} A - \frac{1}{2}\sqrt{\frac{2}{3}} W_1^{\text{lab}} + \sqrt{2} W_2^{\text{lab}} \cos 2\Phi. \qquad (4.2)$$

Here the anisotropic absorbance tensor W^{lab} can be related to the square of the molecular dipole derivatives W^{mol} by[72]

$$W_1^{lab} = \sqrt{3/2}\,a_z = W_1^{mol}\langle S_{11}\rangle + W_2^{mol}\langle S_{12}\rangle$$
$$W_2^{lab} = \sqrt{1/2}(a_X - a_Y) = W_1^{mol}\langle S_{12}\rangle + W_2^{mol}\langle S_{22}\rangle \tag{4.3}$$

with

$$W_1^{mol} = \sqrt{3/2}\left(\mu_{g,\xi}^{(K)}\right)^2$$
$$W_2^{mol} = \sqrt{1/2}\left[\left(\mu_{g,\eta}^{(K)}\right)^2 - \left(\mu_{g,\varsigma}^{(K)}\right)^2\right] \tag{4.4}$$

Here $\langle S_{11}\rangle$ and $\langle S_{12}\rangle$ denote the orientational and transverse order parameters; $\langle S_{21}\rangle$ and $\langle S_{22}\rangle$ reflect the biaxiality of the film. The angle bracket implies that an orientation averaging has been taken with the orientation distribution $f(\Omega)$. For a uniaxial LC film, the resulting infrared absorbance is found to be[25,73-75]

$$A(\Phi = 90°) = A_0\left\langle[-\cos\gamma\cos\phi\sin\beta + \cos\theta\sin\beta\sin\gamma\sin\phi + \cos\beta\sin\theta\sin\phi]^2\right\rangle$$
$$A(\Phi = 0°) = A_0\left\langle[\sin\gamma\cos\theta\cos\phi\sin\beta + \sin\theta\cos\beta\cos\phi + \cos\gamma\sin\beta\sin\phi]^2\right\rangle. \tag{4.5}$$

The infrared dichroic ratio DR can then be calculated with[71]

$$DR = A_X/A_Y = A(\Phi = 0°)/A(\Phi = 90°). \tag{4.6}$$

Note that the direction along $\Phi = 0°$ will not always coincide with the major axis of the IR absorbance ellipse. The averaged orientation of LC molecules is taken to orient with the calculated director profile $(\theta(z), \varphi(z))$ as shown in the inset of Fig. 4.1. This allows us to take into account the effect of the twist deformation in a twisted pi-cell by using Eq. (4.5). In the molecular frame $(\xi\eta\zeta)$, the LC molecules are assumed to possess a degree of freedom in rotation about the molecular ξ-axis. A distribution function $f(\gamma)$ is introduced to describe the LC molecules rotating about the ξ-axis either freely with $f(\gamma) = 1$ or restrained with $f(\gamma) = \cos^2\gamma$.
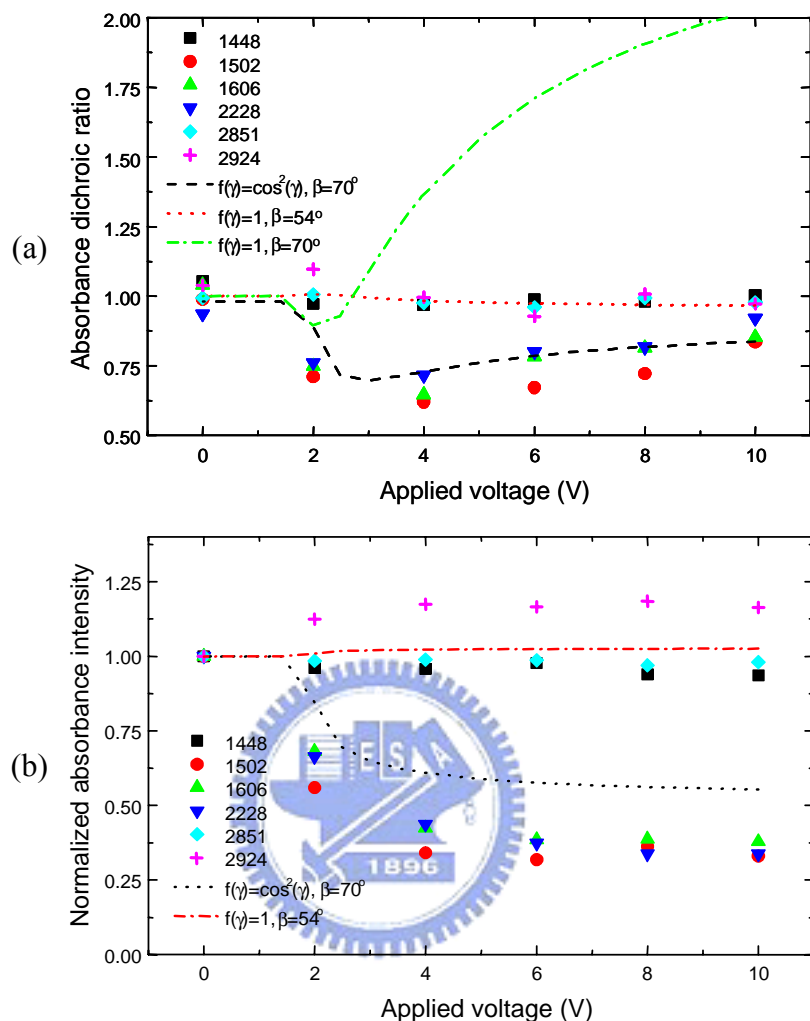
FIG. 4.6. The infrared dichroic ratio (*a*) and the intensity ratio (*b*) of the infrared absorption peaks plotted as a function of voltage. Simulated curves with various orientational distributions of LC molecules are included for comparison.

We found that the stretch modes associated with the LC core at 1502, 1606, and 2228 cm^{-1} can be successfully modeled with $\beta \sim 70°$ and $f(\gamma) = \cos^2 \gamma$ (dashed line). For comparison, the calculated results with a free rotation model are also presented in Fig. 4.6(a) (dashed-dotted curve). Our results appear to indicate that the stretch modes associated with the LC core in the twisted pi-cell agree better with the biased rotation along the molecular long axis. This biased rotation could presumably originate from an interaction of LC molecules with the left-handed chiral dopants. The dichroic ratio of the FTIR peaks associated with the alkyl

chains of the LC molecules shows no clear voltage dependence. For these functional groups, a random distribution with $f(\gamma) = 1$ and $\beta \sim 54°$ is more appropriate in modeling their orientation distribution (see the dotted line in Fig. 4.6(a) and the dashed-dotted line in Fig. 4.6(b)).

4.2.2. Raman Scattering Spectroscopy of Twisted LC Pi-Cells

The Raman spectra taken with a laser polarized along the rubbing direction are presented in Fig. 4.7. As shown by Fig. 4.1, the director of the LC molecules is twisted by 180° along the Z-direction. The order parameter of the C=C stretching mode at 1606 cm^{-1} is therefore decreased from 0.67 in a homogeneously aligned cell to 0.52 in a twisted pi-cell.
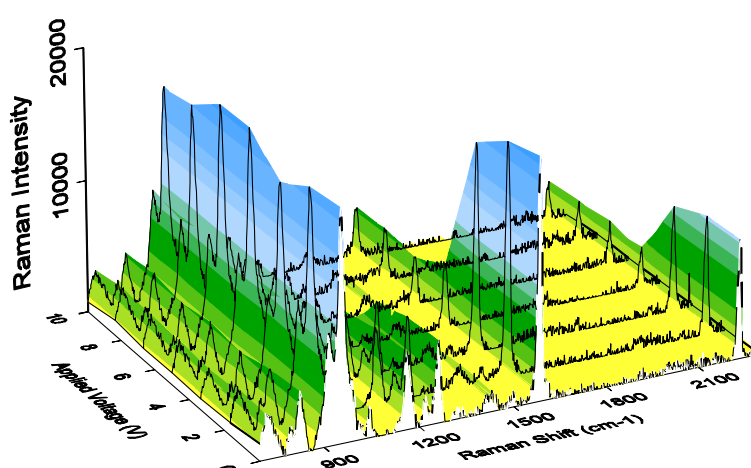
FIG. 4.7. Raman spectra from a twisted pi-cell with varying applied voltage. The polarization of the incident laser beam is parallel to the rubbing direction of the pi-cell.

Several Raman peaks were observed to appear at 705, 790, 821, 957, 1177, 1240, 1285, 1606, and 2228 cm^{-1}, and are summarized in the Table 4.1. The peaks at 705, 790, and 821 cm^{-1} can be ascribed to the C–H out-of-plane wag on the core part of the LC molecule. The angular distortion of the LC core occurs at 957 cm^{-1}. The coupled motions of the C–C inter-core stretch and the C–H in-plane wag

appear at 1177 and 1240 cm^{-1}; the coupling between the C–C intra-core stretch and C–H in-plane wag was found to be at 1285 cm^{-1}. The C=C and C≡N stretching modes produce major peaks at 1606 and 2228 cm^{-1}.

In the C–H stretching region (see Fig. 4.8), two major peaks can be detected at 2851 (s-CH$_2$ stretch) and 2937 (f-CH$_3$) cm^{-1}. Unlike the vibrational features from the LC core, these C–H stretching peaks were found to increase with increasing applied voltage. This result also agrees with the FTIR result presented in Fig. 4.4 and suggests that the planes of the CH$_2$ groups are twisted by the electric field to yield a larger projection on the film surface for the a-CH$_2$ stretching.

It was found from simulation that the LC molecules tilt upward at near 90° when the applied voltage is higher than 4 V. The high polar angle leads to a reduced Raman intensity at 1177, 1285, 1606, and 2228 cm^{-1} with an increasing applied voltage. This can be more clearly seen in Fig. 4.9.
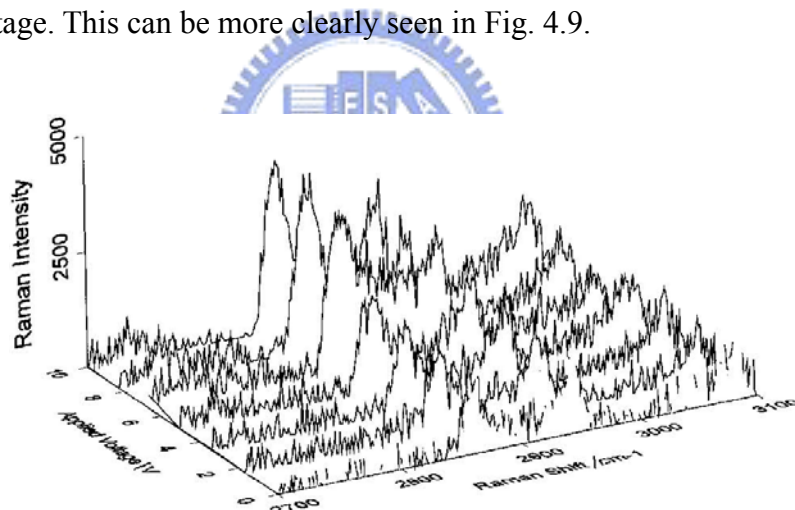
FIG. 4.8. Raman spectra near the C–H stretching region from a twisted pi-cell with varying applied voltages. The incident laser beam is polarized along the rubbing direction of the pi-cell.
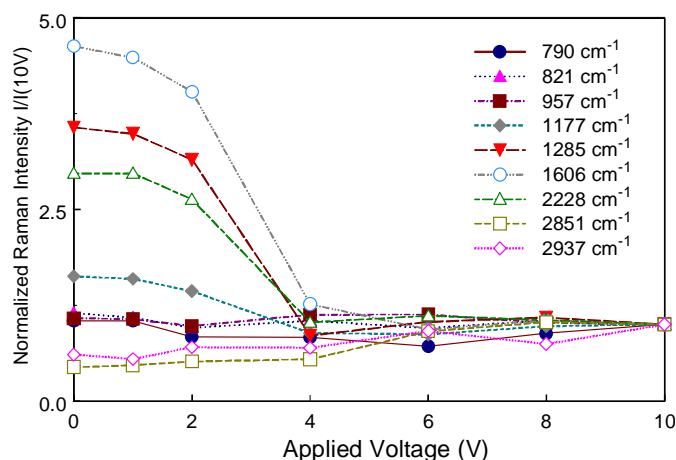
FIG. 4.9. Normalized Raman peak intensities versus applied voltage. The Raman intensities are normalized to the values at 10 V.

4.2.3. Field-Induced Reorientation of Liquid Crystal Molecules in a Twisted Nematic Pi-Cell

To evaluate how fast the twisted pi-cell responds to an electric field, we measured the optical transmittance of the cell with various switching frequencies. Modulated bipolar square waves with 50% duty cycle were employed as the driving field to acquire Fig. 4.10, which presents the results with the drive frequency varied from 50 Hz to 1 kHz. Compared with the measured T-V curve shown in Fig. 4.1, we found that the LC molecules do not return to the 0 V configuration as the drive frequency is higher than 100 Hz. As the drive frequency increases, the duration of the high field envelope (10 V) becomes shorter. At a sufficiently high drive frequency (e.g. 1 kHz), the repetitive high field envelope becomes shorter than the response times of the director. The tilt-up of the LC director driven by the high field and the relaxation back to the low pretilt configuration at 0 V do not have sufficient time to complete. By switching the voltage from 0 to 10 V, the liquid crystal molecules behave as in switching from 5 to 9 V at 500 Hz, and from 6 to 8 V at 1 kHz. The rise time (0% → 90%) of the optical transmittance was measured to be 6 ms and the decay time (100%

$\rightarrow$ 10%) to be about 1.6 ms.
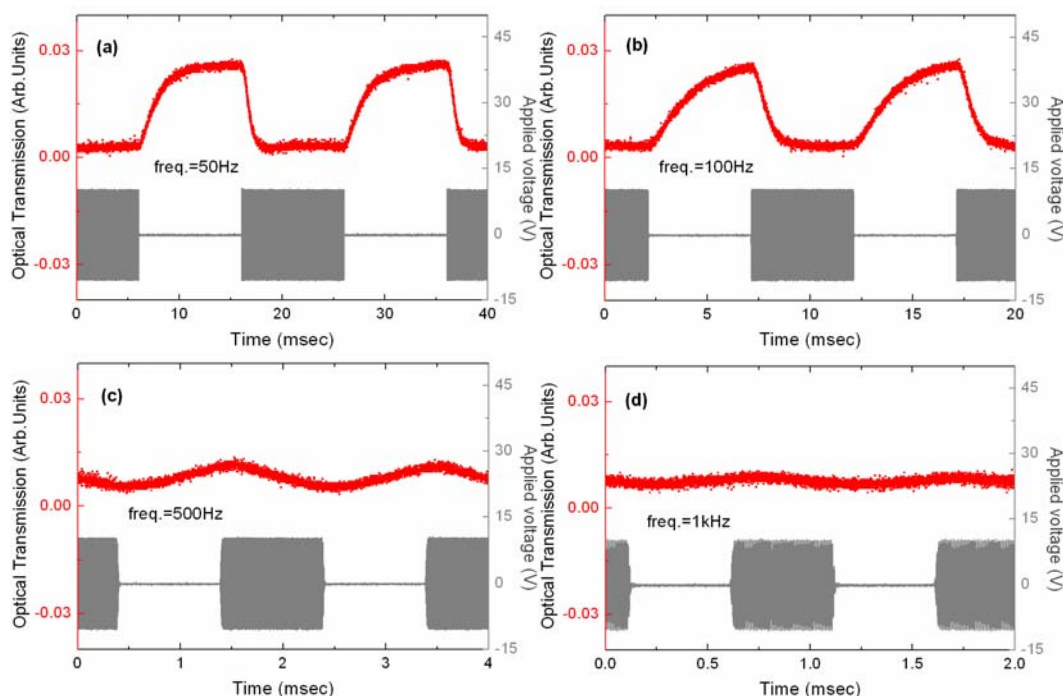
FIG. 4.10. Optical transmission through a twisted pi-cell lying between a set of crossed polarizer and analyzer. The rubbing direction of the cell was oriented 45° relative to the transmission axis of the polarizer. The applied voltage was switched from 0 to 10 V at (*a*) 50 Hz, (*b*) 100 Hz, (*c*) 500 Hz, and (*d*) 1 kHz.

The transient Raman spectra taken from the LC cell during its field-induced switching are presented in Fig. 4.11. A modulated square wave at 500 Hz was applied to the cell. The 10 V amplitude spans from 0 to 1 ms and the 0 V extends from 1 to 2 ms.

The 790 cm^{-1} peak (marked grey), which has been attributed to the C–H out-of-plane wag on the LC core, is significantly enhanced when t > 1 ms. The rapidly changing polar angle of the LC molecules could play a role in yielding the enhanced out-of-plane C–H wag. Similar enhanced responses after switch-off were also found at the CH_2 and CH_3 stretching modes, indicating that LC molecules do not respond to an external field like a rigid molecule. In Fig. 4.12, the applied voltage and the peak intensities at 790, 1606, and 2228 cm^{-1} in Fig.

4.11 are plotted as a function of time. The observed field-induced intensity variations at Raman modes associated with the LC core are strikingly similar to Fig. 4.10(d), indicating the optical response of the pi-cell is dominated by the orientation dynamics of the LC core.
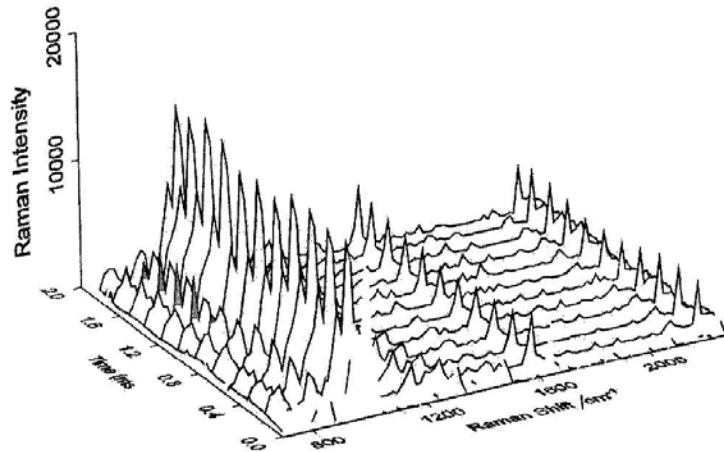
FIG. 4.11. Raman spectra from a twisted pi-cell at varying time. The applied voltage is switched from 0 to 10 V at 0 ms, and 10 to 0 V at 1 ms. The incident laser beam is polarized along the rubbing direction of the cell.
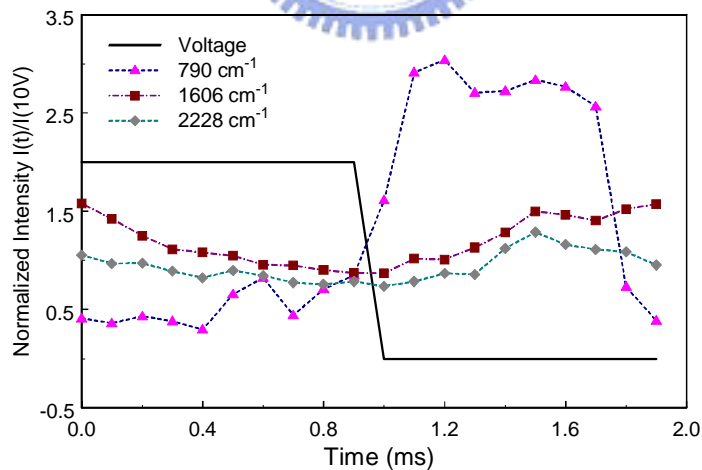
FIG. 4.12. Normalized Raman peak intensities versus time. The applied voltage is switched from 0 to 10 V at 0 ms, and 10 to 0 V at 1ms. The Raman intensities are normalized to the values at 10 V.

4.3. Summary

In conclusion, a twisted nematic liquid crystal pi-cell had been studied in detail by optical techniques including optical transmission measurement, polarized Fourier transform infrared (pFTIR) absorption spectroscopy and Raman spectroscopy. From the pFTIR, the alignment of the LC molecules was revealed and was shown to exhibit a restricted rotation about the molecular long axis. The rise and decay times of the optical response in the twisted pi-cell to an external driving field can be smaller than 6 ms. The switching dynamics was further probed with time-resolved Raman spectroscopy. The vibrational activity of the C–H out-of-plane wag on the LC core was found to be enhanced during the switch-off period. Our data suggest that LC molecules in the twisted pi-cell do not rotate like a rigid molecule during the field-induced reorientation process. The methods used in this study yield valuable information about LC alignment and field-induced reorientation with molecular specificity.